Japanese Journal of Applied Physics **64**, 110801 (2025) **PROGRESS REVIEW**
https://doi.org/**10.35848/1347-4065/ae12fd**

Transition metal monosilicide films on silicon for thermoelectronics and spintronics

Nikolay G. Galkin[1*], Konstantin N. Galkin[1], Dmitrii L. Goroshko[1], Evgenii Y. Subbotin[1], Olga A. Goroshko[1], Igor M. Chernev[1], Andrei M. Maslov[1], Oleg V. Kropachev[1], Semen A. Balagan[1], Sergei A. Dotsenko[1], Anna N. Galkina[1], Dmitry B. Migas[2], Ivan A. Tkachenko[3], Lidiya S. Volkova[4], Timofey S. Grishin[4], and Aleksandr A. Dudin[4]

[1]*Institute of Automation and Control Processes FEB RAS, 690041, Vladivostok, Russia*
[2]*Belarussian State University of Informatics and Radioelectronics, 220013, Minsk, Belarus*
[3]*Institute of Chemistry FEB RAS, 690022, Vladivostok, Russia*
[4]*Institute of Nanotechnology of Microelectronics RAS, 115487, Moscow, Russia*

[*]E-mail: galkin@iacp.dvo.ru

Received August 26, 2025; revised October 3, 2025; accepted October 13, 2025; published online November 3, 2025

The growth of both monoclinic and cubic phases for ultrathin (UT) and thin FeSi and CrSi films and only cubic phase for CoSi on silicon was proven as confirmed by HRTEM. At temperatures of 2–30 K, shunting is absent for the UT films and the two-dimensional conductivity model is realized. In the temperature range of 2–30 K and magnetic fields of 0.25–8 T for the UT films: concentrations and type of majority carriers are determined; NMR and SMR regions are observed in FeSi and CoSi films; quantum MR model is realized in CrSi films at $T = 2$ K. Ferromagnetic loops and a superparamagnetic phase are observed in UT m-FeSi and c-CoSi films from 3 to 300 K. Temperature dependences of the power factor and ab initio calculations of the lattice thermal conductivity of nanowires made it possible to estimate ZT for FeSi and CoSi films as a function of temperature.

Supplementary material for this article is available online

1. Introduction

Transition metal (TM) monosilicides (Cr, Fe and Co) in the form of single crystals and polycrystals have been actively studied for more than sixty years for the purposes of thermoelectronics and microelectronics. It is generally accepted that they have the B20 cubic structure with the space group $P2_13$, exhibiting a variety of optical,[1–3] tunnel-spectroscopic,[4,5] electrical,[6–8] thermoelectric,[1] photoemission,[9] paramagnetic[6,10] and spin (magnetic)[11] properties. It is known that bulk FeSi is a metal, for which a metal-insulator transition with the formation of an indirect band gap from 30 to 60 meV at temperatures below 100 K has been detected in the bulk,[3,4] which is also partially observed for FeSi films, but with a decrease in the band gap width to 8.8–23 meV.[12] An unsolved theoretical problem exists in bulk FeSi indicating the disappearance of the band gap in FeSi when heated above 200 K along with an untypical of classical semiconductors.[13] To explain these phenomena discovered in FeSi, several theoretical approaches were proposed in the 1990s using local density approximation (LDA) calculations, which agreed with each other in the value of the gap (50–110 meV), but diverged in the reasons for the band-gap disappearance at temperatures above 200 K.[1,7,14–21] LDA calculations typically underestimate the band gap, but this is not the case for FeSi, as the band gap is located in the middle of the Fe 3d band, not between different bands.[21] This results in an increase, rather than a decrease, of the calculated band gap compared to experiment.[1,7,14] The problem of the disappearance of the band gap in FeSi upon heating still remains, although several approaches have been suggested to solve this issue: (1) the theory of magnetism of itinerant electrons in a ferromagnetic semiconductor with spin fluctuations;[15,16] (2) the Kondo lattice description with high-temperature magnetism arising from localized magnetic moments of Fe;[7,17] (3) the concept of intermediate valence with ground (spin zero) and excited (spin 3/2) states hybridized with Si;[18] (4) the two-band Hubbard model with local Coulomb interaction (U) to account for the magnetic susceptibility.[19,20]

Chromium monosilicide (CrSi) has been studied mainly from the point of view of transport properties and is known as a resistor material in microelectronics,[22,23] but reports on its electronic, transport and magnetic properties of CrSi are rather scarce.[22–25] It was previously found that bulk CrSi is a paramagnetic metallic material with low resistivity, which depends weakly on the magnetic field.[26,27] But it also has a large positive magnetoresistance and competing ferromagnetic and antiferromagnetic correlations.[28,29] In the case of thin and ultrathin (UT) CrSi films, both ex situ and in situ studies of their transport properties have been published.[30–34] In fact, ex situ studies of UT CrSi films (0.9–2.4 nm thick) grown by solid-phase epitaxy (SPE) with sequential deposition of chromium portions and coated with amorphous silicon (5 nm) on top, in addition to calculations within the two-layer model,[34] revealed metallic conductivity with holes as the main carriers (hole concentration in the layer is $(1–3) \times 10^{13}$ cm^{-2} and mobility is 35–85 cm^2 (V s)$^{-1}$ at $T = 350–550$ K).[34] Theoretical calculations of the cubic structure of CrSi, as a non-magnetic material, were performed within the framework of ab initio methods using the LDA[35] and the generalized gradient approximation (GGR) with spin–orbit coupling.[36] It was found that the Fermi level crosses some bands, which corresponds to their metallic conductivity. The application of the Hubbard-U correction to the Cr-d states in the calculations did not have a significant effect on the band structure of CrSi.[37]

The most interesting material is cobalt monosilicide (CoSi), which in the bulk form is characterized by the violation of the symmetry of spatial inversion in the crystalline cubic lattice and the proximity of the Weyl points to the Fermi level, which characterizes it as a topological Weyl

semimetal from the previously carried out first-principles calculations within the framework of the density functional theory.[38,39] It is also observed that CoSi maintains topological features in a wide energy window around the Fermi level and practically on the entire BZ surface.[38–40] That is, the CoSi system maintains topological features in a wide energy window around the Fermi level and practically on the entire BZ surface.[41] The energy structure of CoSi allows the existence of topological chiral fermions without fine-tuning of the Fermi level.[39] The obtained theoretical results were confirmed experimentally by angle-resolved photoemission spectroscopy (ARPES),[40,42,43] where the band touching nodes in the bulk electron spectrum and the Fermi arcs for CoSi were visualized. The transport, thermoelectric and magnetic properties of thick (100–300 nm) CoSi films on silicon and other substrates have been studied in a small number of studies.[44–48] At the same time, the issue of forming thin (25–70 nm) CoSi films on silicon currently remains poorly understood,[49,50] since the technology for growing epitaxial or textured single-phase CoSi films with similar and smaller thicknesses has not yet been developed. It was found that in amorphous CoSi films the resistivity decreased when the film thickness decreased from 82 to 3.2 nm followed by an increase with a further thickness decrease down to 2 nm.[51] The authors explained the effect of decreasing of the film resistivity by surface-dominated transport associated with topological phenomena, while the observed increase with a further film thickness reduction could be originated from a more complex scattering mechanism to be carefully investigated.[51] However, the transport, magnetoelectric, magnetic and thermoelectric properties of epitaxial and textured UT and thin CoSi films have not been comprehensively studied and compared.

For bulk single crystals of CoSi, FeSi and their ternary alloys $Fe_xCo_{1-x}Si$ the contribution of topological features was confirmed both in electric transport and thermoelectric generation, and in optical properties.[1,6,8,10,11,36,52–56] However, the growth of epitaxial films of TM monosilicides on silicon and the study of the features in their crystal structure, influence of strain with respect to the film thickness on topological and quantum effects have only just begun to be reported.[49,52] For UT films of FeSi[57] and CrSi[58] grown by the SPE method on a Si(111) substrate and not covered with a layer of amorphous silicon, ferromagnetic ordering with a low coercive force was discovered.[59] These layers have low conductivity at temperatures of 2–30 K[12,57,58,60] and an increased Seebeck coefficient (50–200 $\mu V\,K^{-1}$) in the temperature range of 200–400 K.[60] UT FeSi and CrSi films had an increased power factor (2–5 $mW\,m^{-1}\,K^{-2}$).[12] However, the influence of substrate shunting on the Seebeck effect in monosilicide films has not been sufficiently studied, and the thermoelectric properties of thicker films have not been investigated. First-principles calculations of the lattice thermal conductivity of iron monosilicide nanowires made it possible to estimate the value of the dimensionless thermoelectric figure of merit (ZT),[60,61] but without taking into account substrate shunting. For thin CoSi films, a solid-phase growth method was developed,[62] thermoelectric measurements were performed on UT and thin films and lattice thermal conductivity calculations for nanowires were carried out. This made it possible to estimate the value of ZT already taking into account the contribution of shunting by the substrate, but only at individual film temperatures and without plotting ZT as a function of temperature.[63] However, comprehensive studies of the transport, magnetotransport, magnetic and thermoelectric properties of UT and thin films of iron, chromium and cobalt monosilicides on silicon substrates in the temperature range of 3–450 K have not been carried out.

In the above-mentioned works, the crystallization of CrSi, MnSi and FeSi compounds in the cubic B20 structure (space group No. 198, $P2_13$), which do not contain mirror and inversion symmetry,[1,2,6,7] was not questioned. However, the existence of the new ground state in FeSi[57] and CrSi[58] has been shown recently by results of ab initio calculations within a hybrid functional indicating the monoclinic phase (space group No. 4, $P2_1$) which is very structurally close to the B20 cubic one. Moreover, the formation of the monoclinic phase in UT films (3–4 nm) of FeSi and CrSi epitaxially grown on Si(111) silicon substrates by SPE at $T = 350$ °C was also confirmed by high-resolution transmission electron microscopy.[57,58] These UT films had a roughness of less than 0.2 nm with compressive or tensile strain of up to 1.52%–2.69%,[57,58] which ensured a monoclinic distortion of the crystal lattice. By increasing the thickness of FeSi and CrSi films (14–83 nm) formed by molecular beam epitaxy (MBE) at $T = 350$ °C, the formation of the unstrained cubic phase for FeSi[12] and the coexistence of a monoclinic and cubic phase for CrSi were observed.[58] Possible changes in electronic, transport, magnetotransport, magnetic and thermoelectric properties caused by of changing in the type of crystal structure from monoclinic to cubic (or their coexistence) have not been fully investigated.

In this work, our aim is to conduct a general analysis of the crystal structure, transport, magnetic and thermoelectric properties (previously grown and new) of UT (3–5 nm) and thin (10–66 nm) films of Fe, Cr and Co monosilicides formed on silicon substrates with orientations (111) and (001) without covering them with a protective layer. Theoretical calculations of the lattice thermal conductivity of CoSi and FeSi in the form of bulk monocrystals and its nanowires with different diameters and orientations were carried out for the initial assessment of ZT as a function of temperature.

2. Experiment and theory

2.1. Experimental setups and methods

UT and thin films of FeSi, CrSi and CoSi were grown in two ultra-high vacuum (UHV) systems, A-chamber and Varian (both with a base vacuum of 2×10^{-10} Torr). The first UHV chamber was equipped with a low-energy electron diffraction analyzer, a four-sample holder with a direct-current heating system, a quartz thickness sensor, iron, cobalt and silicon sources for deposition of Fe or Co on single-crystal silicon in the SPE method. The second UHV chamber was equipped with a holder for three samples, a quartz thickness sensor and a block of sublimation sources of Fe, Cr, Co and silicon for deposition of Fe (Cr or Co) and Si on single-crystal silicon by either SPE or MBE, a three-coordinate manipulator, a holder for three samples and a quartz thickness sensor. The preparation of silicon substrates (Si (111), FZ1000 and Si(001), FZ2000) and metal sources (Fe, Cr and Co) and silicon for the growth procedure and the

calibration of their deposition rates in both UHV chambers are described in detail in our previously published works.[57,58] The SPE method was used for the growth of UT FeSi and CrSi (at 350 °C) and CoSi (at $T = 500$ °C) films (samples *A, E, I,* Table I). First, Fe (Cr or Co) films of about 2 nm thickness were deposited from a tantalum cell onto an atomically clean Si(111)7 × 7 or Si(001)2 × 2 surface at room temperature (RT) and then annealed at $T = 350$ °C (for FeSi and CoSi) and at $T = 500$ °C (for CoSi) for 2.5–3.0 min. Two samples with UT films of iron and chromium monosilicides (Table I, samples *B* and *F*) were grown on surface reconstructions (SR) of Si(111)2 × 2-Fe and Si(111)$\sqrt{3} \times \sqrt{3}$/R30°-Cr.[33,34] The surface reconstructions were formed by annealing a 0.3 nm thick Fe (Cr) layer at 400 °C for 30 s. These Fe and Cr SRs acted as a seed layer of FeSi or CrSi. Then, Fe (Cr) films with thicknesses of about 2 nm were deposited on top of the PR at RT and annealed at $T = 350$ °C for 2.5 min. Thicker (13.0–66 nm) films (samples *C, D, G, H, K, L, M*, Table I) were grown in a Varian UHV chamber by the MBE method at temperatures of 350 °C (FeSi and CrSi) and 450 °C (CoSi) with different ratios of metal and silicon flows.

One to two hours after unloading from the UHV growth chambers, the morphology of the grown films was examined by atomic force microscopy (AFM) on a Solver P47 scanning probe microscope in the tapping mode. The crystal structure of the grown films was examined by X-ray diffraction on a RIGAKU SmartLab diffractometer (IC FEB RAS) in the 2θ angle range from 5° to 90° with a step of $2\theta = 0.01°$. Some of the UT films were additionally examined by high-resolution transmission electron microscopy (HRTEM) on cross sections using a JEM-2100 (HRP) high-resolution transmission electron microscope at a voltage of 200 kV, characterized by a spatial resolution at points up to lines of 0.16 and 0.1 nm (INME RAS). The lamellae for HRTEM studies were prepared using the focused ion beam (FIB) technique after preliminary deposition of a protective platinum layer from a metalorganic precursor supplied to the chamber of the Helios G4CX electron-ion microscope using a gas injection system. The formed protective layer prevented undesirable effects of the ion beam on the near-surface layers of the formed section. After deposition of the protective layer, local material removal was performed to form a lamella blank, which was then extracted and transferred using a nanomanipulator onto a copper TEM half-grid and fixed using additional platinum deposition. After this, the final thinning of the lamella to a thickness of <50 nm and final polishing at a reduced accelerating voltage were carried out in order to minimize ion-induced structural damage. Using the energy-dispersive X-ray spectroscopy (EDXS) method, element distribution maps and one element distribution profile perpendicular to the film were obtained for the samples, obtained by scanning along a line selected on the sample. The SingleCrystalTM and CrystalMaker® programs were used to determine the axis of the observed zone in the TEM images.[64] Digital processing of the experimental HRTEM images was performed using the Digital Micrograph (GATAN) program.[65]

Electrophysical measurements of magnetoresistance (MR), conductivity, and Hall effect on the grown samples with films and separately on the silicon substrate were carried out by the Waugh-der-Pauw method[13] on a Teslatron TP automated setup with a closed cooling cycle in the temperature range of 2–300 K, magnetic fields with induction from 0.25 to 8.0 T, and a range of operating currents through the sample of 10–100 μA. The linear dependence of the Hall voltage on the magnetic field was checked in the range of 0.25–1.0 T at room temperature. Conductivity and Seebeck coefficient measurements were carried out on a Kriotel setup (made in Russia) in a nitrogen atmosphere in the temperature range of 80–473 K. A two-layer conductivity model was used to take into account the shunting of FeSi, CrSi, or CoSi films by the silicon substrate, and a two-layer thermo-EMF model was used for the Seebeck effect.[66] In this model, a high-temperature-cleaned silicon substrate (effective substrate) has a resistivity and Seebeck coefficient in the temperature range of 80–460 K that differ from those of an uncleaned silicon substrate.[67] This made it possible to calculate the thermoelectric parameters (Seebeck coefficient, resistivity, and power factor) of FeSi, CrSi, or CoSi films as a function of temperature and thickness from the measured Seebeck effect parameters for the film–substrate system (effective values).

Magnetic properties of the samples were studied using a vibrating magnetometer included in the Quantum Design PPMS 9 T ECII physical properties measurement system (Quantum Design International, San Diego, USA). Field dependences were obtained at two temperatures: 300 and 3 (4) K, and in the field range of ±2 T for two magnetic field directions (along the film plane and perpendicular to the film plane). The accuracy of determining the magnetic field and magnetic moment was ±0.01 mT and ±0.1 nA m^2, respectively.

2.2. Ab initio calculations of phonon structure and lattice thermal conductivity

Ab initio calculations of the phonon structure of FeSi and CoSi were carried out within the framework of the density functional theory (DFT) using the GGR with a cutoff energy of 300 eV and using the VASP package.[64,65,68] Gamma-centered k-point schemes were used in the calculations unless otherwise stated, and nonspherical corrections were included. The convergence of the calculations was checked by the cutoff energy and the number of *k*-points. The relaxation of the crystal lattice for FeSi and CoSi was carried out with the *k*-point scheme 12 × 12 × 12. The obtained lattice parameter was 4.430 Å for CoSi and 4.40 Å for FeSi, which is in good agreement with the experimental data: 4.438 Å and 4.4464 Å, respectively.[69] The force constants were calculated within the DFT framework using a supercell of 2 × 2 × 2 unit cells and a 3 × 3 × 3 *k*-point scheme. The phonon structures of bulk FeSi and CoSi were calculated in the harmonic approximation using the Phonopy package.[70] The elements of the dynamic matrix were determined by the finite displacement method using the VASP package. The lattice thermal conductivity, group velocity, scattering velocity, and phonon mean free path were calculated for bulk FeSi and CoSi. The Boltzmann transport equation was solved iteratively using the ShengBTE package.[71] The lattice thermal conductivity of the nanowires was calculated without solving the Boltzmann equation, using the mean free path over all phonon positions in space and the elements of the dynamic matrix calculated for bulk FeSi and CoSi using the ShengBTE package.[71]

Table I. Growth parameters of FeSi, CrSi and CoSi ultrathin and thin films on Si(111) and Si(100) substrates.

Sam-ple	Silicide/substrate	Growth method/T (°C)	d_{Me} (nm)	d_{Si} (nm)	d_{sil} (nm)	σ_{rms} (nm)	XRD (HR TEM) (Refs.)
A	FeSi /Si(111)	SPE/350	2.0	—	3.2	0.3	HR TEM (m-FeSi(111)//Si(111) m-FeSi[$\bar{1}\,\bar{1}$2]//Si[1$\bar{1}$0/ [57)]
B	FeSi /Si(111)	SPE (0.3 nm)/400 + SPE/350	2.3	—	4.3	0.4	XRD (c-FeSi(111)//Si(111))/[57)]
C	FeSi /Si(111)	MBE/350	6.7	8.6	14.0	4.2	XRD (c-FeSi(111)//Si(111))/[12)]
D	FeSi /Si(111)	MBE/350	10.8	13.3	21.3	10.1	XRD (c-FeSi(111)//Si(111))/[12)]
E	CrSi /Si(111)	SPE/350	2.0	—	3.3	0.33	HR TEM (m-CrSi(210)//Si(111) m-CrSi[00$\bar{1}$]‖Si[$\bar{1}$10])/[58)]
F	CrSi /Si(111)	SPE (0.3 nm)/400 +SPE/350	2.3	—	4.1	0.45	HR TEM (m-(c-) CrSi(210)//Si(111) m-(c-) CrSi[00$\bar{1}$]‖Si[$\bar{1}$10])/[58)]
G	CrSi /Si(111)	MBE/350	32	58	66	8.7	XRD (c-CrSi(200)‖Si(111) and m-CrSi(200)‖Si(111))/[58)]
H	CrSi /Si(111)	MBE/350	16.3	23.6	32	0.6	XRD (c-CrSi(200)//Si(111) c-CrSi(200)//Si(111))/[58)]
I	CoSi /Si(001)	SPE/500	2.0	—	3.3	1.0	XRD (c-CoSi(111)//Si(111))
K	CoSi /Si(001)	SPE/500	7.0	—	13.0	1.5	XRD (c-CoSi(111)//Si(111))
L	CoSi /Si(111)	SPE/500	10.0	—	18.0 (14.0 nm from HR TEM)	3.0	XRD (c-CoSi(111)//Si(111)) HR TEM (c-CoSi(111)‖Si(111) c-CoSi[11 $\bar{2}$]‖Si[1$\bar{1}$0])
M	CoSi /Si(111)	MBE/450	17.0	21.4	34.0	10.1	XRD (c-CoSi(111)//Si(111) and c-CoSi(210)//Si(111))

3. Results and discussion

3.1. Morphology and crystal structure features of ultrathin (UT) and thin transition metal (TM) monosilicide films on silicon

After unloading the samples from the ultra-high vacuum chambers, their surface morphology was studied by AFM. It was found that the films of Fe, Cr, and Co monosilicides grown by SPE on silicon have a very smooth surface with a mean-square roughness of 0.3–1.0 nm (Table I, samples *A, B, E, F*, and *I*), which indicates low diffusion mixing at the metal-silicon interface and is confirmed by HRTEM data on cross sections for previously studied FeSi[57] and CrSi[58] films. Films grown by MBE have a higher roughness (Table I, samples *C, D, G, H, K, L* and *M*) due to increased diffusion mixing of two flows of silicon and metal atoms at a low temperature of the silicon substrate (350 °C–500 °C) and 3D nucleation. The crystal structure of UT FeSi and CrSi films according to HRTEM data corresponds to the formation of a monoclinic phase of FeSi and CrSi,[57,58] which coincides with the first-principles theoretical calculations carried out in these papers. For samples *I*, *K* and *L*, in addition to the peaks from the Si substrate (Si(111) and Si (222)) the X-ray diffraction (XRD) spectra also contained 2 peaks from CoSi at 2Θ in the range of 35.05–35.06° and 74.06–74.09° (Appendix A), which correspond to the CoSi (111) and CoSi(222) planes of cubic silicide CoSi of the $P2_13$ space group. Since the XRD spectrum only showed peaks from the parallel CoSi(111) and CoSi(222) planes, it can be concluded that an epitaxial CoSi film consisting of individual nanocrystals (NC) of different thicknesses was formed on these samples. For CoSi NC, the following epitaxial relationship is fulfilled: CoSi(111)‖Si(111). The lattice parameters of CoSi and mechanical strain in CoSi films obtained from the XRD spectra on these samples vary in the range of 0.07%–0.16% with an increase in the thickness of the deposited cobalt from 2 to 10 nm. The data on the cubic structure of CoSi in the films are confirmed by the HRTEM data for sample *L* [Fig. 1(a)] grown by the SPE method. It is clearly seen in the HRTEM patterns [Fig. 1(a)] that the film-Si substrate interface is not atomically smooth. This indicates mutual diffusion of Si and Co atoms during film formation at a temperature of 500 °C (Table I). The consequences of atomic diffusion can be best observed in the atomic distribution profile shown in Fig. 1(c). It is evident that a noticeable concentration of Co atoms is observed in the Si substrate, whereas in the Pt layer formed on the film surface later (before thinning), there are practically no Co atoms. Since the Co concentration is small enough in the Si substrate it does not lead to the formation of Co silicides.

The grown film mainly contains Si and Co atoms [see Fig. 1(c)] indicating the formation of a Co silicide film. The EDX spectrum obtained for the film is shown in Fig. 1(d). The peaks that were used to calculate the concentration of Si and Co atoms are marked in green. It turned out that the concentrations of Si and Co atoms in the film are 47% and 53%, respectively. This means that the grown film is CoSi monosilicide. The increased concentration of Co atoms in the CoSi film suggests that a small portion of the Co atoms was dissolved in CoSi. The thickness of the grown CoSi film is 14 nm [see Fig. 1(a)]. Since the ratio of the thicknesses of the CoSi film and the Co film needed for its formation is approximately 2, so 7 nm thickness of the Co film is used to form the 14 nm thick CoSi. Figure 1(b) shows the fast Fourier transform (FFT) pattern for the region of the CoSi film highlighted by the square white frame in Fig. 1(a). It is evident from the FFT pattern that the CoSi film grew epitaxially on the Si substrate. For CoSi NCs in the grown film, the following epitaxial relationships are satisfied: CoSi $[11\bar{1}]$‖Si$[1\bar{1}0]$, CoSi(111)‖Si(111), which agrees with the XRD data (Appendix A). The interplanar distances for the CoSi(111), CoSi(021), CoSi$(1\bar{1}0)$, and CoSi(201) planes calculated from the FFT pattern are 0.2569, 0.19881, 0.31049, and 0.20285 nm, respectively. Using these interplanar distances, the lattice constant for the cubic CoSi structure was calculated (Table II). Thus, SPE growth of a thin Co film at 500 °C leads to the formation of an epitaxial film of cubic CoSi with a lattice parameter stretched by 1.52% compared to a CoSi single crystal.[69]

With increasing thickness of the FeSi[12] and CrSi[58] films grown by the MBE method, according to the XRD and HRTEM data, grains corresponding to both monoclinic and cubic syngony are observed in the film structure (Table I, samples *C, D, G, H*), which should affect the properties of these films in a wide temperature range. In the thin CoSi film grown by the MBE method at $T = 450$ °C (Table I, sample *M*), according to the XRD data (Appendix A), peaks are observed only from the parallel planes CoSi(111) and CoSi (222) and a very weak peak from the plane $CoSi_2$(222) is weak, which corresponds to the small thickness of the $CoSi_2$ NC. Therefore, it can be stated that the CoSi layer turned out to be epitaxial with the ratio CoSi(111)//Si(111). In this case, the lattice in CoSi NC is practically relaxed.

3.2. Magnetotransport, magnetic and thermoelectric properties of UT and thin TM monosilicide films on silicon: experiment and theory

3.2.1. Transport in the film/substrate system. The main problem of UT and thin films of iron, chromium and cobalt monosilicides on monocrystalline silicon with high resistivity and n-type conductivity is the appearance of the shunting effect. It is necessary to determine a temperature range (usually above 50 K) at which real shunting begins. It is also necessary to answer the question of the effect of ultra-high vacuum cleaning of the silicon substrate at $T = 1150$ °C on the resistivity of the substrate. To assess the conductivity mechanism of UT films of FeSi (samples *A* and *B*), CrSi (samples *E* and *F*) and CoSi (sample *I*) in the film/substrate system and to determine the shunting temperature, the dependences of the sheet resistance of the above samples and the silicon substrate Si(111) before (FZ1000) and after cleaning in ultrahigh vacuum at a temperature of 1150 °C (FZ1000_flash) were plotted [Fig. 2(a)]. It is evident that before the annealing of the silicon substrate at ∼30 K, a sharp increase in the sheet resistance occurs, and at ∼50 K, a minimum of the sheet resistance of silicon and a noticeable intersection with the measurement data of the UT film/substrate systems are observed. However, it is necessary to compare not with a clean substrate before annealing, but with a substrate after UHV cleaning at $T = 1150$ °C. In this case, there is a diffusion of boron atoms from borosilicate glasses in the UHV chamber into the atomically clean silicon surface

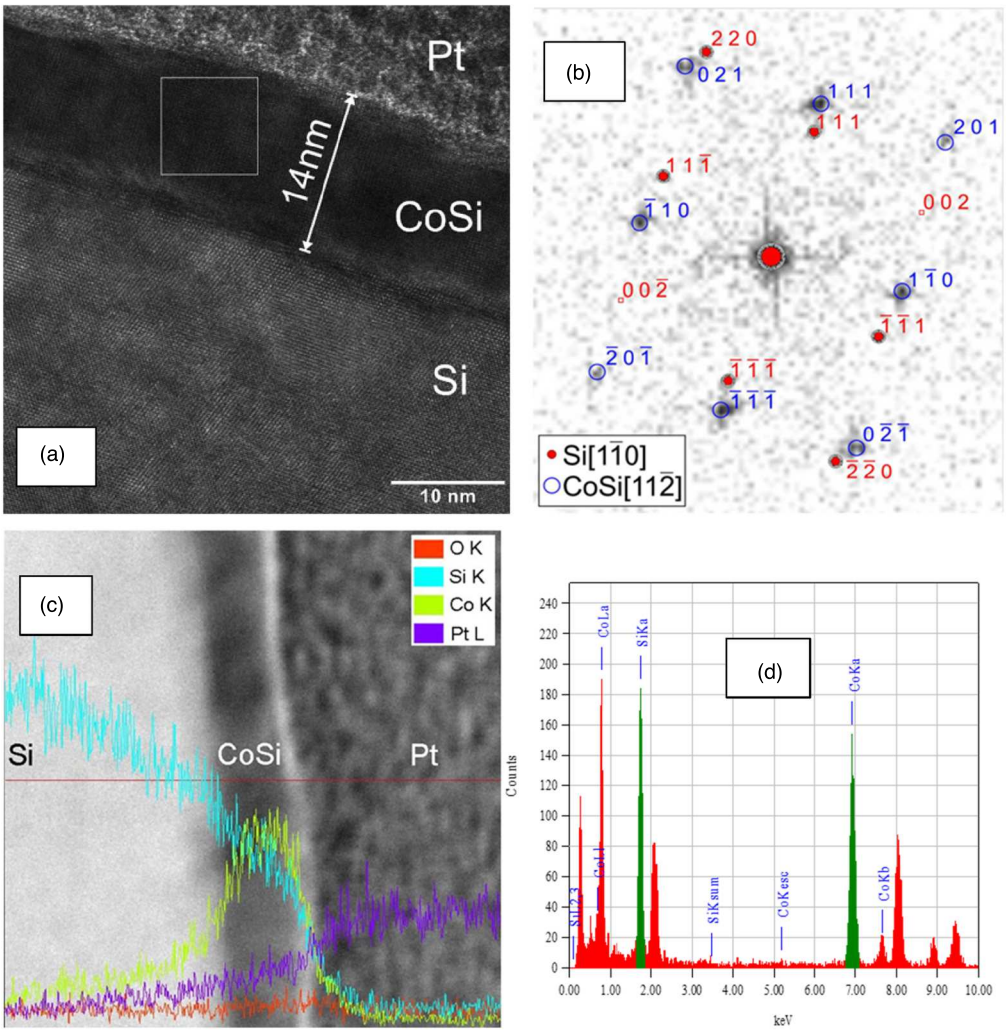

Fig. 1. (a) HRTEM cross-sectional image of sample *L* for the Si[1$\bar{1}$0] zone axis; (b) FFT pattern for the film region highlighted by the square white frame in Fig. 1(a). (c) Distribution profile of Si, Co, Pt, and O atoms obtained perpendicular to the grown film. Scanning was performed along the red line indicated in the bright-field TEM image. (d) EDX spectrum obtained for the film in (a). The peaks used to calculate the concentration of Si and Co atoms are marked in green and red, respectively.

Table II. Lattice constants and lattice mismatch for the crystal structure of CoSi film in relation to the monocrystal CoSi.

Space group and number	Crystal structure	Lattice parameters			Lattice mismatch	
		a (nm)	*b* (nm)	*c* (nm)	direction CoSi[11$\bar{2}$] (%)	direction CoSi[$\bar{1}$10] (%)
$P2_13$ (#198)	Simple cubic	0.44556	—	—	1.51	1.52

with the formation of a p-layer with a depth from hundreds of nm to units of microns depending on the annealing duration that unavoidably leads to the formation of the p–n junction with a n-type Si substrate.[67] The effective sheet resistance of such a double silicon layer increases, which is seen in the graph of Fig. 1(a). In this case, it can be stated that the sheet resistance of the UT film-substrate system in the temperature range of 50–300 K is 2–4 times lower than that of such a silicon substrate. This does not allow us to completely exclude shunting at these temperatures, but allows us to state that complete freezing of carriers occurs in silicon at temperatures below 30 K. At temperatures of 2–30 K for UT films of Fe, Cr and Co monosilicides, linear dependences of sheet resistance on lnT are observed, which, according to the data of Ref. 72, corresponds to the two-dimensional nature of conductivity in UT films regardless of the type of their crystal structure. At the same time, for the UT CoSi film, the sheet resistance is 2–4 times higher than that for UT FeSi and CrSi films. Based on the structural data, the UT FeSi, CrSi and CoSi films are epitaxial (Table I) and exhibit a relatively weak dependence of surface resistance on temperature (2–30 K), which corresponds, taking into account its actual thickness, to the properties of a metal with high resistivity exceeding the Mott–Ioffe–Regel limit.[73]

For thin FeSi, CrSi and CoSi films (Samples *C, D, G, H, K, L* and *M*), the dependence of the sheet resistance in the film/substrate system on temperature (2–450 K) is plotted in a linear scale [Fig. 2(b)]. The most distinctive dependence is exhibited in the case of FeSi (samples *C* and *D*) indicating a smooth increase in the sheet resistance with decreasing temperature from 150 to 50 K, associated with a metal-semiconductor transition and the opening of an indirect band

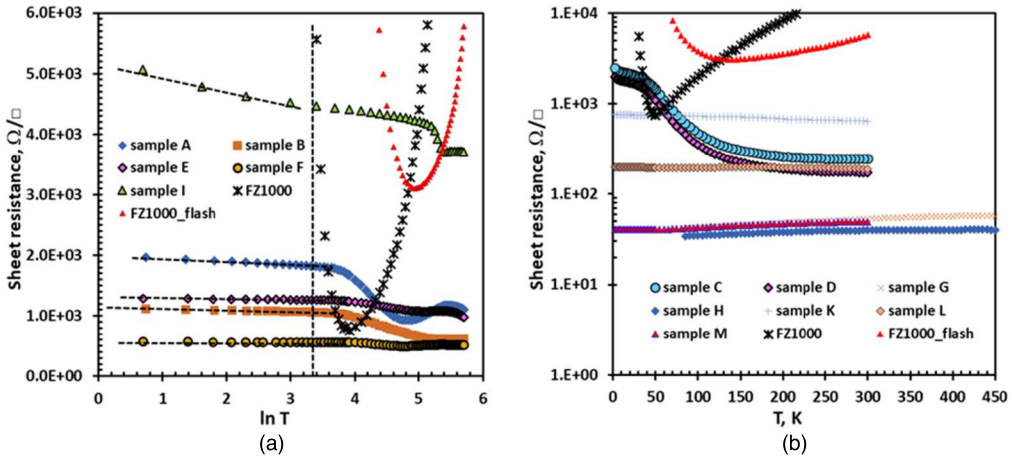

Fig. 2. Sheet resistance versus lnT for samples *A, B, E, F* and I (a) and temperature dependence of the sheet resistance for samples *C, D, G, H, K, L,* and *M* (b). All samples have ultrathin (a) and thin (b) FeSi, CrSi and CoSi films on silicon substrates. Sheet resistance temperature dependences shown also for original Si(111) substrate (FZ1000) and Si(111) substrate after pulsed annealing under ultra-high vacuum conditions (FZ1000_flash).

gap with a width of about 23 meV.[12] At temperatures below 30 K, a reverse transition to the region of two-dimensional metallic conductivity is observed (shunting is absent). The sheet resistance for chromium (Samples *G* and *H*) and cobalt (Samples *K, L* and *M*) monosilicides weakly depends on temperature. Samples *G* and *H* with thin CrSi films demonstrate a slight decrease in sheet resistance with decreasing temperature from 450 to 80 K and with values from 60 Ω/□ to 40 Ω/□ [Fig. 2(b)], which corresponds to the weak metallic nature of their conductivity. The maximum sheet resistance (760 Ω/□) is observed for a thin film in sample *K* (CoSi) with a thickness of about 13 nm (Table I), which increases very slightly at temperatures from 300 to 2 K. A similar dependence on temperature is demonstrated by sample *L* with a CoSi film with a thickness of 14 nm [Fig. 1(a)] and a maximum sheet resistance of about 200 Ω/□ [Fig. 2(b)]. For sample *M* with a CoSi film, a smooth decrease in sheet resistance is observed with decreasing temperature, which corresponds to the transition of the film to a conducting state with a decrease in sheet resistance by about 5 times (40 Ω/□) compared to sample *L* [Fig. 2(b)]. That is, CrSi and CoSi films with thicknesses from 32 to 66 nm pass into a conducting state and do not depend on the shunting by the silicon substrate. At film thicknesses of 13–14 nm, a partial effect of shunting is observed, which must be taken into account when analyzing the results of magnetotransport, Hall and thermoelectric measurements.

As shown above, UT films of Fe, Cr and Co monosilicides grown on Si(111) and Si(001) substrates showed some unusual transport properties in a wide temperature range. However, in the temperature range of 2–30 K these UT films have a characteristic small (from 2% to 7%) increase in sheet resistance (decrease in sheet conductivity), which is not typical of ordinary metals. The values of resistivity, taking into account the real thickness of the films ($(4–9) \times 10^{-4}$ Ω cm), lie above the maximum resistivity for metals ($3–5) \times 10^{-4}$ Ω cm, characterized as the Mott–Ioffe–Regel limit.[73] For continuous UT films, it is more likely due to the two-dimensional conductivity mechanism[72] than to the variable-length hopping conductivity mechanism,[13,34] which involves Coulomb interaction through a gap near the Fermi level between localized electrons.

Thin FeSi, CrSi, and CoSi films with thicknesses of 13–66 nm (Table I) consist of intergrown grains of both the cubic phase (c-FeSi, c-CrSi, c-CoSi) and the monoclinic phase (m-CrSi) together with the cubic (c-CrSi).[58] In this case, the resistivity $(1.3–2.5) \times 10^{-4}$ Ω cm is slightly less than the minimum conductivity in the Mott–Ioffe–Regel limit,[73] so the conductivity mechanism may differ from the two-dimensional one.[72]

Since UT films consist of epitaxial grains (some of them with different orientations), they introduce scattering of carriers at grain boundaries and defects. Therefore, to analyze transport properties, one can apply the theory of two-dimensional conductivity based on the model of a two-dimensional electron gas in a non-activated quasi-metallic medium with the effects of electron–electron interaction and disorder,[74–76] and apply it to UT films, as was done in Ref. 72. According to this model, a power-law dependence of the surface conductivity of the film on temperature is assumed:

$$\sigma_{\square}(T) = \sigma_{\square}(T_o) + (N_{el} \times e^2/(\pi \times h)) \ln (T/T_o) \qquad (1)$$

where $\sigma_{\square}(T)$ and $\sigma_{\square}(T_o)$ are the sheet resistances at T and T_o temperatures; e is the charge of electron; h is the Planck constant; and N_{el} is the coefficient. However, this model does not consider localization effects,[72] which can influence the change in conductivity at ultra-low temperatures.

For the theory of electron–electron interaction,[74] the constant N_{el} in formula (1) is given by the expression:

$$N_{el} = 0.5(1 - F) \qquad (2)$$

where F depends on the ratio of the Fermi wavelength to the screening length. The constant F approaches 1 for strong screening and 0 for weak screening.[72]

The main problem in the model is the determination of the critical temperature (T_o),[72] since it can differ in two-dimensional films of different metals. In our experiments, a linear dependence of the sheet resistance on the logarithm of the temperature was observed for all studied UT films of monosilicides for temperatures below 30 K [Fig. 2(a)]. Therefore, to calculate the change in the sheet conductivity of these films, we also consider $T_o = 30$ K as the initial temperature. Changes in the sheet conductivity ($\Delta\sigma_{\square}$) are

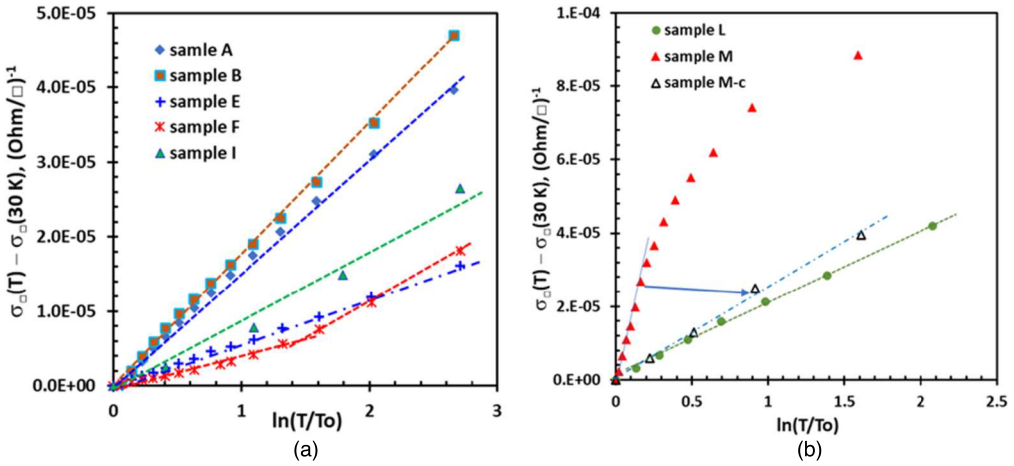

Fig. 3. The dependence of sheet conductivity changes ($\Delta\sigma_{\square} = \sigma_{\square}(T) - \sigma_{\square}(T_o)$) versus $\ln(T/T_o)$ at $T = 2$–30 K for UT FeSi, CrSi and CoSi films in the samples *A, B, E, F* and *I* (a), and for the CoSi thin films in the samples *L* and *M* (b). Critical temperature is $T_o = 30$ K. Linear approximations of the experimental data UT and thin films are represented by the dashed lines. "Sample *M*-c"—is the sample with another $T_{o1} = 10$ K.

shown in Fig. 3(a). For FeSi films in samples *A* and *B*, linear dependences of the change in sheet conductivity on $\ln(T/T_o)$ are observed in the whole range (2–30 K) [Fig. 3(a)], which corresponds to the mechanism of two-dimensional conductivity in the films. In this case, the maximum change in the sheet conductivity is at least 7%. Calculations of the coefficient N_{el} in Eq. (1) showed that for the film in sample *A* it was equal to 1.436, and to 1.21 for the film in sample *B*. These values are larger than 1 and therefore, within the framework of the model, correspond to a strong electron–electron interaction. The values more than 1.0 in the model[72] may correspond to localization effects, which will be considered below. For the CrSi film in sample *E* [Fig. 3(a)] a linear dependence of the change in sheet conductivity ($\Delta\sigma_{\square}$) on $\ln(T/T_o)$ is also observed. Calculation from the slope of the coefficient N_{el} gives the value of $N_{el} = 0.48$, which corresponds to the value of the coefficient $F = 0.04$ and therefore, in this film, there is no electron–electron interaction. In the CrSi film of sample *F*, two slopes are observed [Fig. 3(a)]. We will consider the smaller slope, which begins at the point $\ln(T/T_o) = 0$, as the base slope. According to Eq. (1), it corresponds to the constant $N_{el} = 0.306$ at $F = 0.008$. This also confirms the weak electron–electron interaction in this film. The presence of the second section corresponds to the constant $N_{el} = 0.736$ and $F = 0.47$, which indicates an increase in the electron–electron interaction due to some structural rearrangements. According to the HRTEM data, the monoclinic m-CrSi phase was detected in the film of sample *A*, and the film of sample *B* consists of grains of both c-CrSi and m-CrSi.[58] Thus, the appearance of two linear sections in Fig. 3(a) is associated with different contributions to the conductivity at different temperatures of charge carriers belonging to m-CrSi and c-CrSi. In the UT film of sample *I*, a quasi-linear dependence of the change in sheet conductivity ($\Delta\sigma_{\square}$) on $\ln(T/T_o)$ is observed [Fig. 3(a)] with averaged coefficients $N_{el} = 0.73$ and $F = 0.46$, which indicates an increased electron–electron interaction in the UT CoSi film grown.

Here, it is also necessary to note the specific influence of the predominant phase in UT films on the value of sheet resistance [Fig. 2(a)] and on the sheet conductivity [Fig. 3(a)]. The highest sheet resistance is exhibited by samples with a predominant contribution of the monoclinic phase for both FeSi (sample *A*) and CrSi (sample *E*) [Fig. 2(a)]. In the case of pre-formation of iron and chromium surface phases on silicon before monosilicide growth, only the cubic phase forms in the UT FeSi film (sample *B*), while in the UT CrSi film (sample *F*), the contribution of the cubic phase becomes predominant. In both cases, this leads to a twofold decrease in sheet resistance with an increase in film thickness of no more than 30%. This indicates higher sheet conductivity of the cubic phases of monosilicides compared to the monoclinic phases in the UT FeSi and CrSi films. Furthermore, FeSi films exhibit higher sheet conductivity compared to CrSi films, which is due to the observed stronger electron–electron interaction.

With increasing thickness of the CoSi film (14 nm), grown by the SPE method at a temperature of 500 °C, the linear dependence of $\Delta\sigma_{\square}$ on $\ln(T/T_o)$ is preserved [Fig. 3(b)], which emphasizes the two-dimensional nature of its conductivity. But the calculation of the coefficient N_{el} gave a value of 1.63, which led to a strong increase in the coefficient $F = 2.26$ (modulo), which is significantly greater than 1 and indicates a strong electron–electron interaction.

In a thicker CoSi film (34 nm), a strong nonlinearity of the $\Delta\sigma_{\square}$ dependence on $\ln(T/T_o)$ is observed at $T_o = 30$ K [Fig. 3(b), sample *M*], which corresponds to a deviation from the two-dimensional conductivity mechanism along the film and a transition to a three-dimensional conductivity mechanism. However, a small linear part is retained for a small temperature range and requires a separate analysis, which has been carried out using a reduced initial temperature ($T_{o1} = 10$ K) [see the designation of sample *M*-c, Fig. 3(b)]. In this case, the linearity of the dependence of $\Delta\sigma_{\square}$ on $\ln(T/T_o)$ is restored, which means the absence of shunting and the two-dimensional nature of conductivity at temperatures below 10 K. At the same time, the constants $N_{el} = 1.99$ and $F = 2.98$ (modulo)increased indicating an increase in the electron–electron interaction, probably due to the opening of an additional conductivity channel along the surface at ultra-low temperatures, associated with surface-dominated transport caused by topological phenomena, as in the work for thin CoSi films.[44] According to low-temperature conductivity data, topological effects in UT FeSi and CrSi films are not observed.

3.2.2. Magnetotransport properties of UT TM monosilicide films. Due to the complexity of presenting of the results of magnetotransport measurements on the magnetic field and temperature in a single graph, we will first consider three sets of field dependences of magnetoresistance (MR) ($MR_{xx} = [R_{sh}(H) - R_{sh}(0)]/R_{sh}(0)$), where R_{sh} is the sheet resistance) for UT m-FeSi (sample *A*), m-CrSi (sample *E*) and cubic CoSi (sample *I*) films [Figs. 4(a)–4(c)] in the temperature range assuming two-dimensional conductivity (2–30 K). Since there is no shunting of the film by the substrate in this temperature range, all the observed effects are associated only with UT films. For a 3.0 nm thick m-FeSi film (sample *A*) at $T = 2$ K, negative MR (NMR) is observed in fields up to −1.3 T and +1.9 T [Fig. 4(a)]. With the increase of magnetic field more than 2 T for $T = 2$ K monotonic positive MR (PMR) occurs with the value of MR_{xx} up to 0.2%–0.22%. At $T = 10$ K non-monotonic NMR with the maximum of −0.055% at $B = 2.5$ T and the transition to PMR at 6.5 T is observed. At 20 and 30 K monotonic NMR is evident, reaching −(0.10–0.12)% at ±8.0 T. The m-FeSi film (sample *A*) has in common the presence of NMR, which with the increase of magnetic induction passes into PMR for 2 and 10 K, but remains so at 20 and 30 K. Linear dependences for PMR and NMR are not observed at all temperatures.

For the UT m-CrSi film in sample *E* at $T = 2$ K, a very small NMR with an amplitude of up to −0.02% and a magnetic induction of up to ±(1.2–1.5) T is present [Fig. 4(b)]. At fields above 2.0 T, a PMR is evident with a linear increase in the MR_{xx} value to 0.30% at $B = \pm 8.0$ T. At $T = 10$ K and a magnetic induction of up to ±2.0 T, a practically zero value of MR_{xx} is detected with a noticeable noise amplitude of up to ±0.02%. With an increase in magnetic induction above 2.0 T, a PMR is observed with a quasi-linear increase in the MR_{xx} value to ±0.12% [Fig. 4(b)]. At temperatures of 20 and 30 K, the situation is partially the same, but the close to zero MR_{xx} values are maintained up to $B = \pm 4.0$ T, and with an increase in the magnetic field induction, the PMR increases quasi-linearly to approximately 0.03%.

For sample *I* with the UT CoSi film [Fig. 4(c)] the nature of the magnetoresistance field dependences changes. At a temperature of 2 K and magnetic induction up to ±3.6 T, approximately symmetrical regions with NMR with a maximum value of up to −0.08% are observed. With an increase in magnetic induction above 3.4 T, an intersection of the ordinate axis and a transition to the PMR region with a maximum value of MR_{xx} up to 0.22% at $B = 6.0$ T are revealed. At temperatures from 5 to 30 K, only symmetrical dependences of PMR on magnetic induction (from quadratic to linear) are detected. The maximum value of $MR_{xx} = \pm 0.45\%$ is observed at $T = 5$ K for $B = \pm 6$ T followed by a decrease in PMR with an increase in temperature. The minimum value of PMR is observed at 30 K with a linear dependence of MR_{xx} on magnetic induction [Fig. 4(c)].

Let us consider how the character of the field dependences of magnetoresistance changes in the temperature range of 2–30 K with an increase in the film thickness using the example

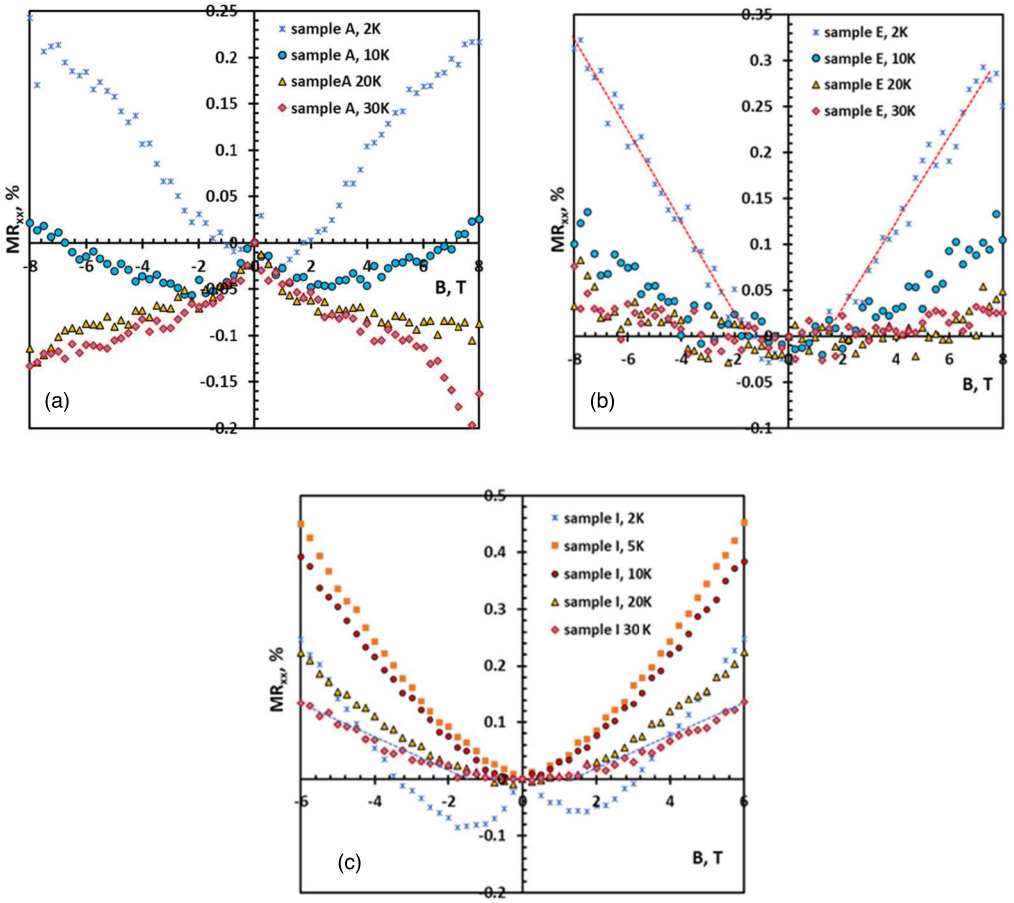

Fig. 4. Magnetoresistance (MR_{xx}) for samples *A*, *E* and *I* with ultrathin films of FeSi (a), CrSi (b) and CoSi (c) versus magnetic induction in the temperature range of 2–30 K.

of samples *C* and *L* with thin FeSi and CoSi films (Fig. 5), respectively. For the FeSi film [Fig. 5(a)] the character of the dependences has slightly changed when observing the regions of the NMR and PMR as well as crossovers between them, but the main issue is in increased MR_{xx} values. At a temperature of 2 K, near-zero values of MR_{xx} are noticeable up to $B = \pm 1.0$ T, and with its increase to ±6.0 T, linear dependences with a maximum value of ±2.0% are observed. Similar behavior of the field dependences can be seen at 5 K. But up to $B = \pm 2.0$ T, symmetrical regions of the NMR are visible with a further transition to PMR at a magnetic induction of more than 2.4 T and preservation quadratic dependence on the magnetic induction. In the temperature range of 10–30 K, only the NMR regions with different MR_{xx} values are detected. However, for $T = 10$ K, a quadratic law of magnetic field variation without transition to PMR is characteristic. When moving to temperatures of 20 and 30 K, a change in the nature of the RM_{xx} dependence on induction from quasi-linear to linear with a maximum of −1.3% at $B = \pm 6.0$ T can be noted [Fig. 5(a)]. For a thin CoSi film (sample *L*), regions of very weak NMR with symmetric parts from 0 T are observed only at 2 K to ±3.4 T [Fig. 5(b)]. At magnetic induction above 3.4 T, a transition to the PMR region with a quadratic dependence on induction occurs. At temperatures from 10 to 30 K, symmetrical quadratic MR_{xx} dependences are observed with a maximum value of up to 0.1% at ±8.0 T. In this case, a decrease in the MR_{xx} values is seen with an increase in temperature from 10 to 30 K [Fig. 5(b)]. Comparison of Figs. 4 and 5 shows that with an increase in thickness, the most noticeable changes in the field dependences of magnetoresistance are typical of thin CoSi films.

As shown by the studies of magnetoresistance (MR_{xx}) in UT and thin FeSi, CrSi and CoSi films (Figs. 4 and 5), at temperatures below 30 K, various effects occur. At temperatures below 10 K, regions of NMR, PMR and their crossovers are observed at different magnetic fields. The appearance of linear sections up to 8 T instead of the quadratic MR dependence on the magnetic field (Fig. 4) were also detected in this range. Since for UT and thin films the temperature range above 40 K are associated with the redistribution of currents between the film and the substrate, i.e. with the shunting effect, this range is not considered. Magnetoresistance is characterized by the classical dependence of magnetoresistance on the square of the magnetic field ($\mu H < 1$):[77)]

$$\frac{\Delta\rho}{\rho} = \begin{cases} (\mu H)^2, \ \mu H < 1 \\ C, \ \mu H > 1 \end{cases}. \tag{3}$$

But below 30 K in the UT m-CrSi film [Fig. 4(b)] a gradual transition to the quantum limit regime is observed, when the energy of the quantum level exceeds the Fermi energy, and the holes occupy the lowest quantum state of transverse motion in the magnetic film according to the Abrikosov model.[78)] For semimetals, which are characterized by shallow valleys of charge carriers near the Fermi level with a high concentration (in our case $(2.7–3.5) \times 10^{21}$ cm^{-3} at 2–30 K, see appendix B) of charge carriers and their low mobility,[79)] this quantum limit can be reached at fairly weak magnetic fields, in contrast to narrow-gap semiconductors such as InSb.[80)] For the UT m-CrSi film, the quantum magnetoresistance is positive, non-saturated and linear in very low fields and is observed only at 2 K. Moreover, the weak antilocalization associated with the negative magnetoresistance is absent in this case [Fig. 4 (a)].[72)]

For UT and thin FeSi films, only the PMR branches are observed in the dependences of magnetoresistance on the magnetic induction value [Figs. 4(a) and 5(b)] at a temperature of 2 K. As the temperature increases from 10 to 30 K, both the NMR and PMR regions are visible, as well as crossovers on the ordinate axis from the NMR to the PMR with an increase in the modulus of magnetic induction. Such behavior is typical of the alternation of the effect of weak localization (the PMR region) and weak antilocalization (the NMR region),[1,7)] which characterizes quantum processes leading to additives in conductivity.[81)] A more detailed analysis of these processes in UT m-FeSi and thin FeSi films is planned to be carried out in an article that will be presented separately.

In the UT c-CoSi film, the dependence of magnetoresistance on magnetic induction [Fig. 4(c)] shows a local low-amplitude region of the NMR at fields up to ±3.4 T, which corresponds to the appearance of quantum processes at ultra-low temperatures that affect the conductivity.[1,7,81)] With increasing temperature, a transition to the PMR region occurs, with the maximum MR_{xx} observed at $T = 5$ K, followed by a decrease in the MR_{xx} value with increasing

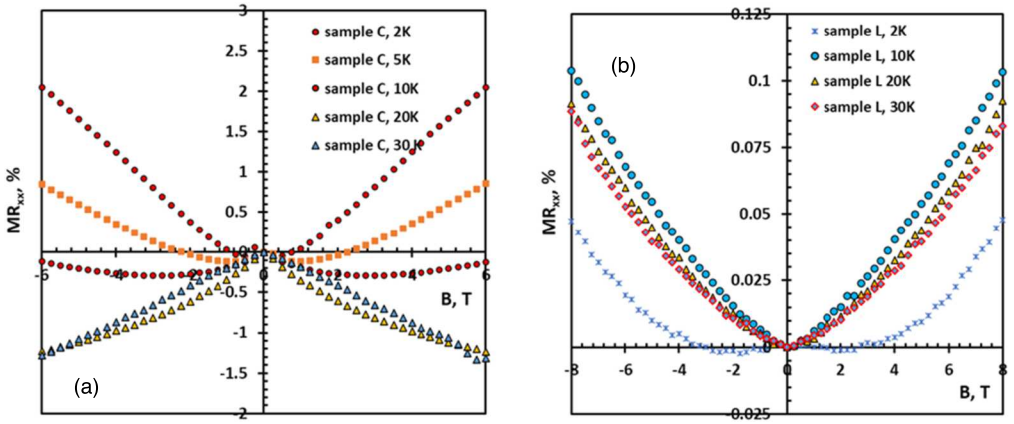

Fig. 5. Magnetoresistance (MR_{xx}) for samples *C* and *L* with thin films of FeSi (a) and CoSi (b) versus magnetic induction in the temperature range of 2–30 K.

temperature. At $T = 30$ K, linearity of the MR_{xx} dependences on magnetic induction (in modulus) is observed, as in the UT m-CrSi film, which is most likely associated with a decrease in the MR_{xx} value and an increase in measurement errors.

To check the implementation of the normal Hall effect for samples *A* and *K* with FeSi and CoSi films, respectively, after the Hall measurements, the dependences of the Hall resistance ($R_{xy}(B) = R_{xy}(B) - R_{xy}(0)$) on the magnetic field induction from −6.0 to +6.0 T [Figs. 6(a), 6(b)] at temperatures from 2 to 40 K were calculated. Figure 6(a) shows these dependences for the UT of the m-FeSi film in sample *A*. It is seen that in the temperature range from 2 to 30 K the dependences are linear and pass through zero, which corresponds to the absence of the anomalous Hall effect for the film.[13] At 40 K, the appearance of a nonlinear characteristic $R_{xy}(B)$ is observed, corresponding to the onset of the anomalous Hall effect due to the participation of carriers from the silicon substrate with a built-in p–n junction. The slope of the dependences is positive pointing out the hole type of conductivity.[13] On the contrary, for the c-CoSi film in sample *K*, a negative slope is observed with electrons as the main charge carriers. And the linearity of the $R_{xy}(B)$ dependence also indicates the implementation of the normal Hall effect in the c-CoSi film up to 40 K, which corresponds to the predominant transport along the film at this temperature.

Since the characteristic properties of the UT films of m-FeSi (sample *A*), m-CrSi (sample *E*) and c-CoSi (sample *I*) can be accurately determined only in the temperature range below 30 K, the temperature Hall measurements for the UT films of these monosilicides have been carried out for these samples in the magnetic induction range from 0.25 to 8.0 T [Figs. 7(a)–7(c)]. For the m-FeSi film in sample *A*, no changes in the positive Hall coefficient (R_H) with temperature are observed at a fixed magnetic induction [Fig. 7(a)], which corresponds to the preservation of the concentration of holes as main charge carriers.[13] At the same time, its positive value decreases with increasing magnetic induction by more than 1 order of magnitude, which corresponds to an increase in the hole concentration in the FeSi film from 7×10^{19} cm^{-3} ($B = 0.25$ T) to 1.0×10^{21} cm^{-3} ($B = 8.0$ T). In the m-CrSi film (sample *E*) at temperatures of 2–30 K, the positive Hall coefficient is also preserved [Fig. 7(b)], but with a value two orders of magnitude smaller than in the UT m-FeSi film at $B = 0.25$–0.5 T. A further increase in magnetic induction leads to an additional decrease in the Hall coefficient, i.e. an increase in the carrier concentration (mainly holes with a concentration of 3×10^{22}–6×10^{22} cm^{-3}, see appendix B).[13] The appearance of negative values of the Hall coefficient at a magnetic induction of 0.25–0.5 T [Fig. 7(b)], apparently, corresponds to random errors in measuring small Hall voltages. At the same time, at 40 K, a sharp increase in the positive Hall coefficient is observed [Fig. 7(b)], which indicates the onset of shunting of the CrSi film by the silicon substrate and coincides with the data of the $R_{xy}(B)$ dependence at this temperature [Fig. 6(a)].

For the UT c-CoSi film, a different character of the dependences of the negative Hall coefficient (electrons)[13] on the magnetic induction and temperature is detected [Fig. 7(c)]. At temperatures of 2–10 K, a strong increase in the Hall coefficient in modulus is observed with an increase in the magnetic field at the specific temperature, which corresponds to a decrease in the electron concentration and is confirmed by calculations [Fig. 7(d)]. It should be noted that at $T = 2$ K and weak magnetic fields (0.25–0.5 T), the main carriers are holes, which correlates with the appearance of the positive Hall coefficient at this temperature during Hall measurements [Fig. 7(c)] and is associated with the weak localization process.[1,7] At temperatures from 5 to 10 K and a magnetic field smaller than 1.0 T, the sign of the majority carriers changes to negative, that is, electrons with a concentration of 6×10^{21}–3×10^{22} cm^{-3} [Fig. 7(d)] become the main carriers. At temperatures from 5 to 10 K and a magnetic field of more than 1.5 T, the sign of the main carriers conserves negative (electrons with a concentration of $(3–6) \times 10^{21}$ cm^{-3} [Fig. 7(d)]), but the positive magnetoresistance [Fig. 4(c)] occurs. Thus, in the UT c-CoSi film at 2 K, the main effect on carrier transport is exerted by weak localization of carriers, whose concentration decreases due to the growth of magnetic induction to ±3.5 T. At 30 K, the dependence of the electron concentration on the magnetic field completely disappears and the main mechanism becomes the quantum limit regime in accordance with the Abrikosov model,[78] when the energy of the quantum level exceeds the Fermi energy, and the electrons in the c-CoSi film occupy the lowest quantum state of transverse motion in the film.

3.2.3. Magnetic properties of TM monosilicide films. Let us consider magnetic properties in UT films of

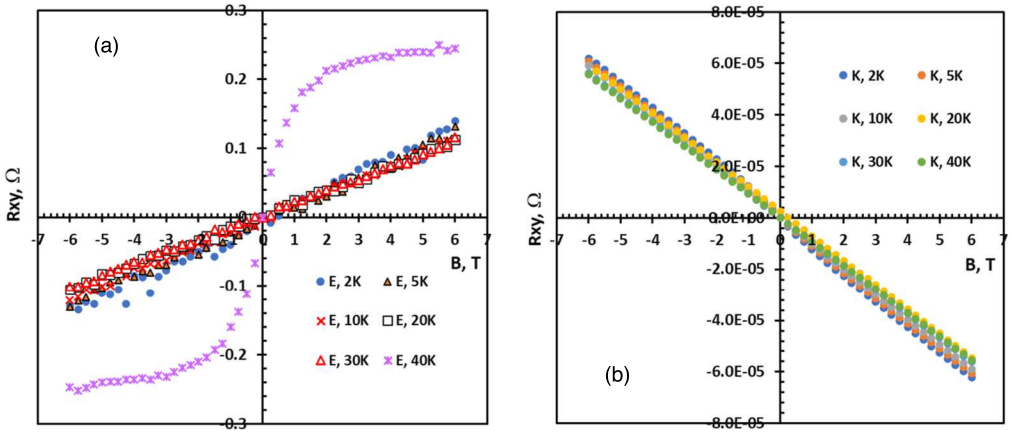

Fig. 6. Hall resistance (R_{xy}) versus magnetic induction and at low temperatures (2–40 K) for samples *E* and *K* with UT m-CrSi film (a) and thin c-CoSi film (b) on the Si(111) substrate.

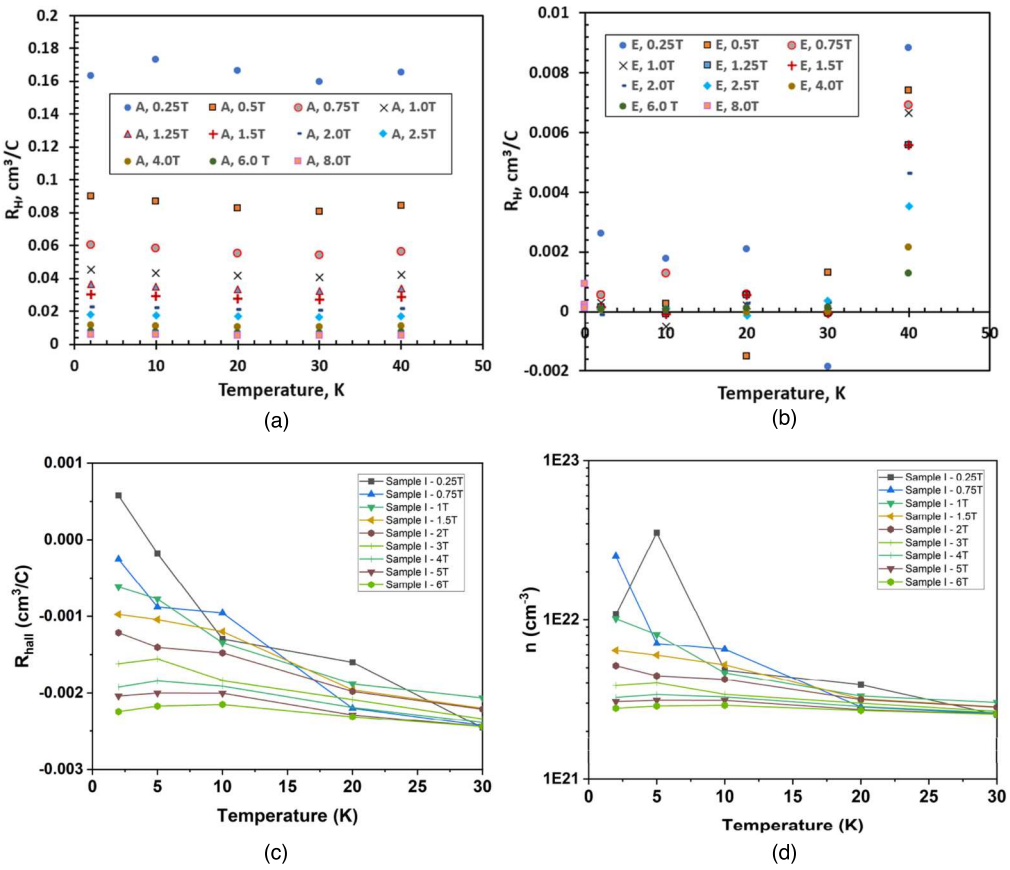

Fig. 7. Hall coefficient (R_H) dependence versus temperature range (2–40 K) for samples *A* (a), *E* (b) and (*I*) with ultrathin films of FeSi (a), CrSi (b) and CoSi (c) at the magnetic induction range of (0.25–8.0) T. The temperature dependence of carrier concentration (electrons) for CoSi film in the sample *I* (d).

iron, chromium and cobalt monosilicides. Since the films are ultra-thin and the silicon substrate is diamagnetic with a much larger volume of material by mass, it is necessary to take into account this diamagnetic substrate contribution and the errors in measuring very small magnetic moments near the sensitivity limit of the Quantum Design PPMS 9 T ECII setup. In our previously published article,[57] it was shown that after subtracting the diamagnetic contribution of the substrate the UT m-FeSi film in sample *A* (Table I) exhibited ferromagnetic properties with perpendicular anisotropy, a saturation magnetic moment of 3.4 nA m^{-2} or 2.0 μ_B and a low coercive force of 0.05 mT, both at a temperature of 4 K and at $T = 300$ K. Therefore, the UT m-FeSi film was characterized as an ultrasoft ferromagnet with perpendicular anisotropy, which is atypical of bulk c-FeSi, which is a non-magnetic material.[6,10] An additional study of the field dependence of the magnetic moment at 4 K and room temperature in a magnetic field of up to 200 mT showed the asymmetry of the FM loops due to presence of both ferromagnetic and antiferromagnetic (AFM) phases in the m-FeSi film. This issue correlates with the data of first-principles calculations also carried out in Ref. 57. Carrying out temperature cooling in a magnetic field (FC) and without a magnetic field (ZFC) showed the appearance of a blocking temperature of about 70 K indicating the presence of a phase with spin glass properties in the m-FeSi film, having different FM–AFM ordering.[57]

Magnetic properties in the UT m-CrSi film (sample *E*) were also investigated and analyzed in our work.[59] Measurements of the magnetic moment of the sample with the film and subtraction of the contribution of the diamagnetic substrate showed that at 3 K, FM loops with noticeable noise were observed in the film plane (in-plane) and perpendicular to it (out-plane), which had an insignificant (12%–15%) difference in the saturation magnetic moments: 5.8 nA m^2 or 3.05 μ_B (out-plane) and 5.1 nA m^2 or 2.68 μ_B (in-plane).[59] At 300 K, the measurement errors increased with a simultaneous decrease in the magnetic moment values upon saturation and preservation of the FM loops: 2.0 nA m^2 or 1.05 μ_B (out-plane) and 2.5 nA m^2 or 1.32 μ_B (in-plane).[59] At both temperatures, the FM loops had small coercive forces of 0.001–0.01 T[59] pointing out ferromagnetic ordering and metallic conducting behavior in the UT m-CrSi film [Fig. 2(a)]. The experimentally estimated values of the magnetic moments at 3 K[59] were quite close to the theoretically predicted values at 0 K (2.1 μ_B for the FM phase of c-CrSi and 2.8 μ_B for the AFM phase of m-CrSi).[58,59]

The field dependences of the magnetic moment for sample *I* with an UT c-CoSi film were studied in the range of magnetic induction $B = \pm 1.0$ T [Fig. 8(a)]. Also, after measurements with a magnetic field along the film and subtracting the contribution of the silicon substrate, the formation of an FM loop was detected both at room temperature and at 4 K. At 300 K the magnetic moment reached saturation (7.0 nA m^2 or 3.68 μ_B) at 0.3 T with virtually zero coercive force [Fig. 8(a)]. Despite the higher saturation magnetic moment (by one and a half to two times) compared to UT m-FeSi and m-CrSi films, the noise during measurements is strong, which indicates the effect of

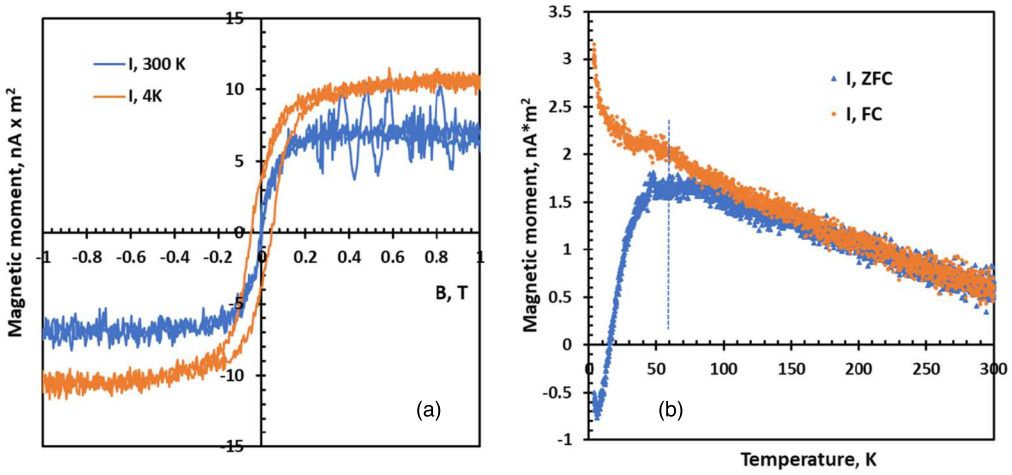

Fig. 8. (a) Magnetic field dependencies of the magnetic moment for the in-plane magnetic field at 4 and 300 K for the UT c-CoSi film (the *I* sample). (b) Temperature dependences of magnetization using cooling techniques in zero (ZFC) and non-zero (FC) magnetic fields (50 mT).

temperature on the magnetization process. At $T = 4$ K, an increase in the saturation magnetic moment to 10.4 nA m^2 or 5.47 μ_B at $B = 0.60$ T is observed, a coercive force of about 0.04 T and a residual magnetization of about 4 nA m^2 (or 2.1 μ_B) appear, but the noise does not completely disappear. The residual magnetization indicates that at low temperatures, all grains of the UT c-CoSi film do not have time to undergo magnetization reversal at zero magnetic field.

Studies of the temperature dependence of the magnetic moment for UT c-CoSi film upon cooling in a magnetic field of 50 mT (FC) and without a magnetic field (ZFC) [Fig. 8(b)] showed that the FM ordering was maintained up to 100 K, and then the magnetic moment begins to decrease and rapidly decreased at below 60 K (the blocking temperature). This corresponds to the transition of the CoSi film to the blocking region of superparamagnetism,[82)] which is associated with the existence of nanosized grains whose magnetic moment decreases at low temperatures and may correspond to the spin glass state.[83)]

Let us consider the differences in the behavior of a thin (34.0 nm) c-CoSi film (sample *M*) in a magnetic field. At two temperatures (4 and 300 K), the magnetic moment was studied in a magnetic field (in the film plane) from −3.0 to +3.0 T [Fig. 9(a)]. After subtracting the contribution of the substrate,[84)] it is seen that at both temperatures, FM loops are observed with virtually no noise, and at room temperature, saturation of the magnetic moment (5.6 nA m^2 or 3.38 μ_B) is achieved at an induction starting from 2.0 T. The coercive force is zero, as for the UT c-CoSi film in sample *I* at 300 K [Fig. 8(a)]. On the contrary, at 4 K, saturation of the magnetic moment is not observed up to 3.0 T. At maximum induction, the value of ±13.5 nA m^2 or 7.1 μ_B is found. The coercive force reaches 0.1 T, and the residual magnetic moment is ±4.5 nA m^2 or 2.37 μ_B. Thus, in a thin CoSi film, the number of magnetic domains capable of aligning along the magnetic field increases at minimum temperature, and at room temperature their contribution decreases. Let us consider how a thin CoSi film behaves when cooled in a magnetic field of 50 mT (FC curve) and without a magnetic field (ZFC curve) [Fig. 9(b)]. Its behavior is similar to that of the UT CoSi film [Fig. 8(b)], but the magnetic moment increased in a magnetic field at 4 K–3.7 nA m^2 or 1.95 μ_B, and the blocking temperature decreased to 45 K. The decrease in the magnetic moment upon cooling without a magnetic field started at 80 K, which indicates the beginning of blocking of the contribution of superparamagnetic particles in the thin c-CoSi film.

Since the magnetic properties of UT and thin FeSi and CrSi films have been considered in detail in our previous publications[57,58)] and the main result for them is the manifestation of weak ferromagnetic and antiferromagnetic properties that are not inherent in bulk iron and chromium monosilicides,[6,10,85)] we will focus on discussing the magnetic properties of UT and thin c-CoSi films (Figs. 8 and 9). Two experimental facts should be noted: (1) observation of ferromagnetic loops from ultralow temperatures (3 K) to room temperature (300 K) and (2) the appearance of a blocking temperature on the FC curves, which correlates with the data for the UT m-FeSi film.[57)] For UT and thin c-CoSi films at room temperature, the coercive force is close to zero similar to a superparamagnet.[82)] But at 3 K it increases to 0.04 T for the UT c-CoSi film [Fig. 8(b)] and to 0.1 T for the thin c-CoSi film [Fig. 9(b)]). And the blocking temperature, on the contrary, decreases from 60 to 45 K with increasing thickness. In the case of the UT c-CoSi film, a broadened peak shape is observed [Fig. 8(b)] and complete demagnetization below 10 K, taking into account the possible error in subtracting the diamagnetic contribution of the silicon substrate,[84)] which was characterized as a wide distribution of magnetic nanoparticles by size in Refs. 86, 87. For the thin c-CoSi film [Fig. 9(b)] the peak with the blocking temperature became narrower, which may indicate a smaller width of the distribution of nanoparticles by size. In our experiments, both with UT m-FeSi films and with UT c-CoSi films, such nanoparticles, according to the HR TEM data for m-FeSi films[57)] and c-CoSi film [Fig. 1(a)] have sizes of tens of nanometers. With such sizes,[82)] nanoclusters are unlikely to be the cause of superparamagnetic effect in the grown films of iron and cobalt monosilicides. Another reason for this phenomenon may be metal atoms dissolved in the monosilicide lattice, but they do not form nanoclusters with sizes of units of nanometers visible in HR TEM images on Fig. 1(a) and in work.[57)] At the same time, according to the EDX data [Figs. 1(c), 1(d)] the concentration of excess (according to the CoSi

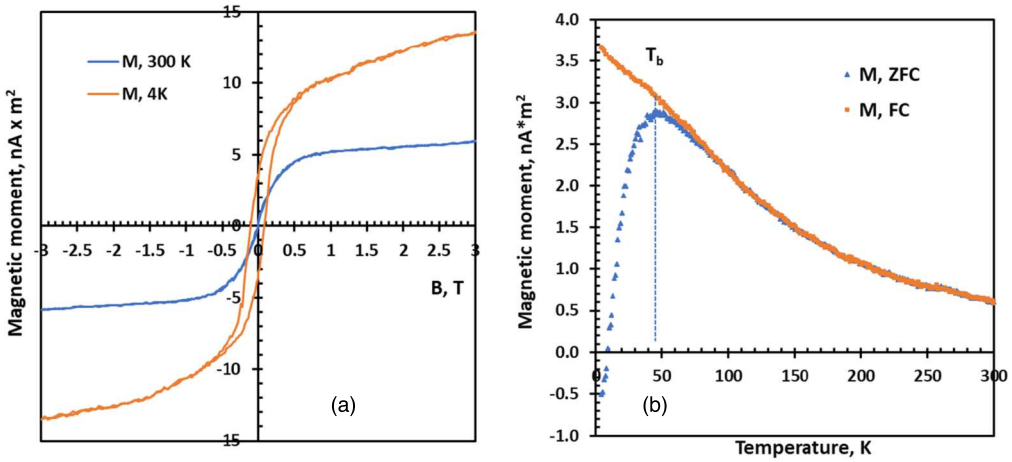

Fig. 9. (a) Magnetic field dependencies of the magnetic moment for the in-plane magnetic field at 4 and 300 K for the thin CoSi film (the *M* sample). (b) Temperature dependences of magnetization using cooling techniques in zero (ZFC) and non-zero (FC) magnetic fields (50 mT).

stoichiometry) cobalt atoms are 1%–2%. Since both films in samples *I* and *L* have been grown by the SPE method at 500 °C, this allows us to assume that the amount of dissolved cobalt changes proportionally to the thickness of the deposited cobalt, and then the dissolved cobalt atoms cannot be the cause of the observed superparamagnetic effect. For 4 K, the magnetic moment is not saturated to 3 T and increases by about 1.3 times, i.e. not proportionally to the thickness (a 10 fold difference between thin and UT c-CoSi films), and a noticeable coercive force and residual magnetic moment also appear [Fig. 9(a)], which does not allow us to classify the considered m-FeSi[57] and c-CoSi films as classical superparamagnets. A possible reason for the occurrence of superparamagnetism in these films may be structural defects in nanoclusters (vacancies, interstitial atoms and dislocations), which leads to the occurrence of bound magnetic polarons in accordance with the RKKY model,[88] in which localized magnetic moments interact through exchange with delocalized electrons, as was concluded in the work for ZnO nanoparticles doped with Ag and Ni atoms.[86] However, in the case of FeSi and CoSi semimetals, this requires additional research.

The analysis of the obtained results showed possible applications of UT films of iron, chromium and cobalt monosilicides on silicon:

(1) The UT m-FeSi film on silicon is an ultrasoft ferromagnet with perpendicular anisotropy at room temperature without residual magnetization. In a longitudinal magnetic field and upon cooling, the UT m-FeSi film exhibits FM-AFM properties, which allows us to consider it as an example of a combination of a ferromagnet and a spin glass with FM-AFM order.

(2) The UT m-CrSi films have soft ferromagnetic properties (s-FM) with a noticeable residual magnetization in the plane (0.5 M_{sat}) at 300 K, so they can be used as a longitudinal magnetic field sensor.

(3) Thin c-CoSi films on silicon exhibit superparamagnetic properties with a blocking temperature of 45–60 K, but retain ferromagnetic properties with a noticeable coercive force and residual magnetic moment at helium temperatures, which is promising for the creation of highly sensitive and low-temperature magnetic field sensors.

3.2.4. Thermoelectric properties of the film/substrate systems and contribution of the TM monosilicide films. In Sect. 3.2.1 it was shown that UT m-FeSi, m-CrSi and c-CoSi films have the metal conductivity only at temperatures below 30 K, and at higher temperatures they begin to be shunted by the silicon substrate, so the thermoelectric properties for samples with UT films were not studied. Thermoelectric properties were studied in detail only for thin monosilicide films (Table I) that have noticeable conductivity and conductivity temperature dependences different from those of silicon [Fig. 2(b)]. The results of the thermoelectric measurements were presented for them in the form of temperature dependences of the effective sheet resistance [Fig. 10(a)], the effective Seebeck coefficient [Fig. 10(b)] and the effective power factor [Fig. 10(c)] for films of iron (samples *C* and *D*), chromium (samples *G* and *H*) and cobalt (samples *K* and *L*) monosilicides and the silicon substrate (FZ1000) after its annealing under ultrahigh vacuum conditions.

From Fig. 10(a) it is evident that samples *G*, *H* and *L* with thicknesses respectively of 66, 32 and 14 nm possess the minimum sheet resistance. FeSi film have relatively low sheet resistance up to 250 K, which then rapidly increases due to metal-semiconductor transition.[12] Sample *K* with c-CoSi films with thickness of about 13 nm has the highest sheet resistance (Table I). However, the sheet resistance of all samples with films is significantly (by one to one and a half orders of magnitude) lower than the sheet resistance of silicon substrate after ultrahigh vacuum cleaning at 1150 °C. Figure 10(b) shows temperature dependences of effective Seebeck coefficient for monosilicide films on the silicon substrate and silicon after UHV cleaning. The behavior of the effective Seebeck coefficient for silicon (change of sign from positive to negative at 440 K) confirms the formation of a p-layer on the surface of n-type silicon. At the same time, samples with thin FeSi and CrSi films have a positive effective Seebeck coefficient [Fig. 10(b)], which does not change its sign with increasing temperature and is in the range of 50–80 $\mu V\,K^{-1}$. This corresponds to the main contribution of holes to the effective Seebeck coefficient, as the main carriers in films of different thicknesses. For samples *K* and *L* with CoSi films, on the contrary, the effective Seebeck coefficient is negative in the whole

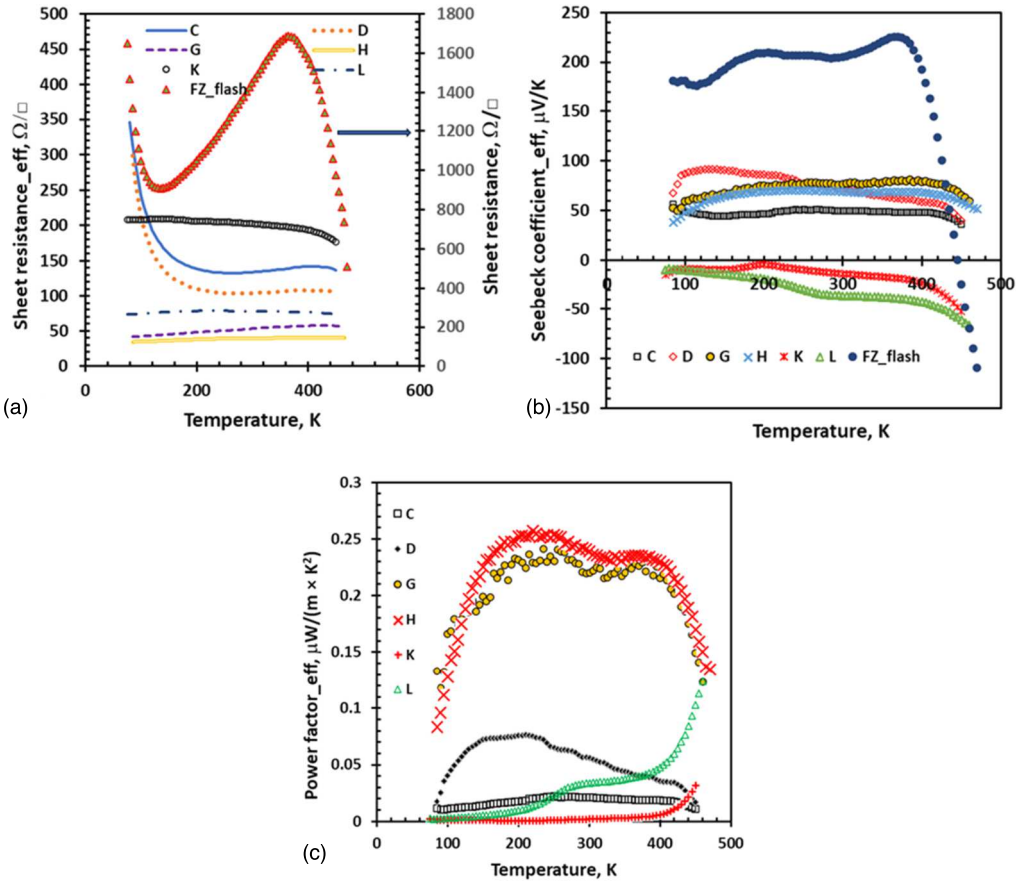

Fig. 10. Temperature dependences of (a) effective sheet resistance ($R_{\square}$), (b) effective Seebeck coefficient (S), and (c) effective power factor (S^2/ρ) for samples *C, D, G, H, K* and *L* with thin FeSi, CrSi and CoSi films (Table I). For the high-temperature annealed Si substrate (effective substrate or FZ_flash), only $R_{\square}$ and S dependences are shown.

temperature range [Fig. 10(b)] indicating electrons as the main charge carriers. The analysis of the data of the thin film/substrate showed that in the range of 75–400 K the main contribution was made by carriers in monosilicide films, while the contribution of the substrate was found to be significant at 400–460 K. Therefore, it is possible to calculate the parameters of the films themselves using a two-layer thermo-EMF model[66] and involving data on the Seebeck coefficient and conductivity, which were measured separately in additional experiments.

The calculations performed are shown in Fig. 11 as temperature dependences of the resistivity, Seebeck coefficient and power factor for films in samples *C, D, G, H, K* and *L*. The calculations showed that CrSi (sample *H*) and CoSi (samples *K* and *L*) films have the minimum resistivity. It is practically independent of temperature in the range of 80–460 K and is in the range from 70 μΩ cm (sample *L*) to 150–200 μΩ cm (samples *H* and *K*) [Fig. 11(a)]. The positive Seebeck coefficient is the largest (50–80 $\mu V\,K^{-1}$) for samples *D* (c-FeSi), *G* (c-CrSi + m-CrSi) and *H* (c-CrSi) [Fig. 11(b)]. The maximum decrease in the positive Seebeck coefficient with decreasing temperature is observed for sample *C* with the minimum thickness (14 nm) for the continuous c-FeSi film (Table I), which is probably due to the role of boron and silicon atoms from the substrate, but requires separate analysis. For c-CoSi films, a negative Seebeck coefficient is observed in samples *K* and *L*, the modulus of which was slightly adjusted upward in accordance with their thicknesses. The calculations of the power factor [Fig. 11(c)] showed that the maximum values are observed for samples *H* and *K* with c-CrSi and c-CoSi films, respectively, in the temperature range of 200–400 K. The obtained power factor values for them are in the range of 2.5–2.8 $mW\,m^{-1}\,K^{-2}$. At temperatures below 200 K, they gradually decrease to 1.0–1.5 $mW\,m^{-1}\,K^{-2}$. For sample *L* with a 14 nm thick c-CoSi film, a different character of the dependence is observed with an increase from hundredths to tenths of a $mW\,m^{-1}\,K^{-2}$ from 80 to 200 K. With a further increase in temperature, an intensive increase in the power factor to 2.8 $mW\,m^{-1}\,K^{-2}$ is found in the temperature range of 200–460 K [Fig. 11(b)]. In the c-FeSi film in sample *D* (thickness in 21.3 nm), a bell-shaped dependence of the power factor on temperature is revealed with a maximum of 1.4 $mW\,m^{-1}\,K^{-2}$ at 220 K [Fig. 11(c)]. In sample *C* with a 14 nm thick c-FeSi film, the power factor smoothly increases with increasing temperature and reaches 0.5 $mW\,m^{-1}\,K^{-2}$ at 460 K [Fig. 11(c)]. Despite the maximum thickness (66 nm) in the c-CrSi + m-CrSi film (sample *G*) a weak dependence on temperature and small values of the power factor from 0.5 to 0.7 $mW\,m^{-1}\,K^{-2}$ are observed. Next, we will analyze how the film thickness affects the achievable power factor for the grown films.

3.2.5. Estimation of *ZT* value for CoSi and UT and FeSi thin films based on lattice thermal conductivity of its nanowires. Thin films of CoSi and FeSi showed a noticeable power factor [Fig. 11(c)], but their applicability as thermoelectric materials depends on both the lattice thermal conductivity and the contribution of charge carriers to the

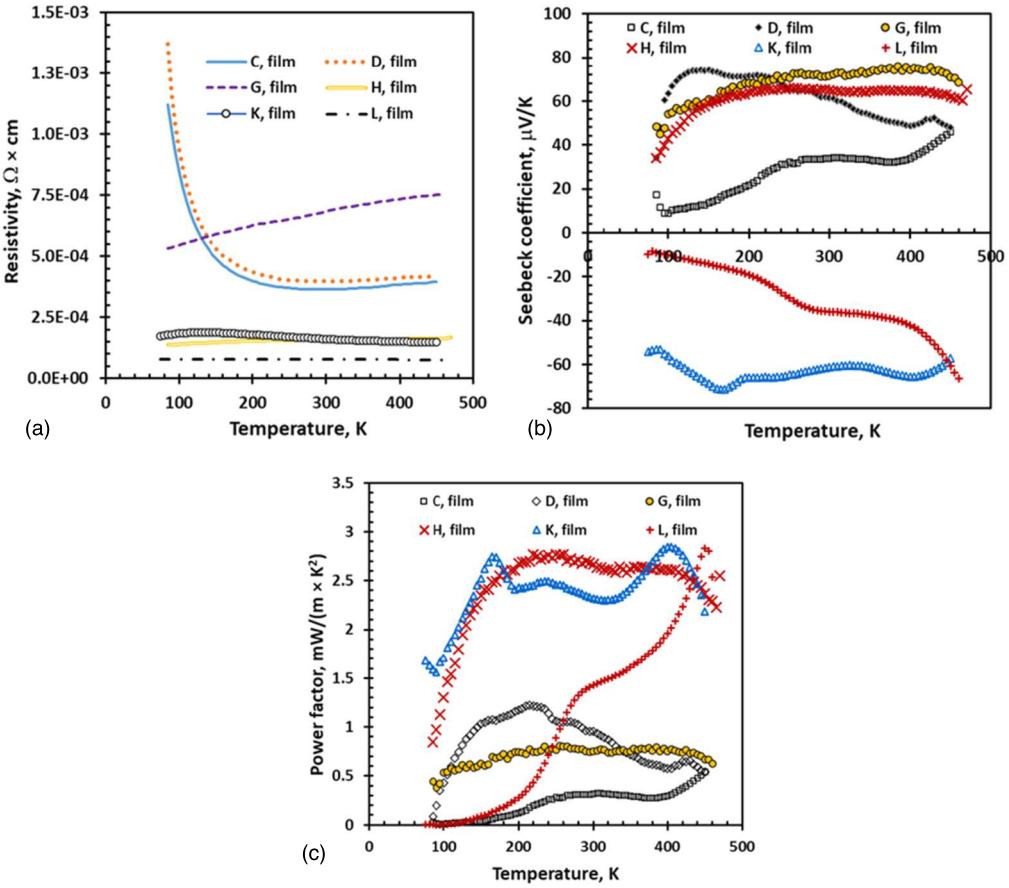

Fig. 11. Temperature dependences of (a) resistivity (ρ) for FeSi, CrSi and CoSi thin films samples *C, D, G, H, K* and *L* (Table I) (left axis) and effective substrate (right axis), (b) Seebeck coefficient (*S*), (c) power factor (S^2/ρ).

thermal conductivity. Preliminary calculations for both systems showed that the phonon structures of both FeSi and CoSi in the bulk state are stable compounds, which is confirmed by the absence of imaginary frequencies.[54,56)] The calculations of the lattice thermal conductivity for c-FeSi and c-CoSi single crystals carried out in this work using the methods described above are in good agreement with the literature data (30–60 $W\,m^{-1}\,K^{-1}$) for bulk FeSi and CoSi.[89,90)] Since there are no experimental data on the thermal conductivity of thin films of TM monosilicides, the main issue in the calculations is to establish the effect of spatial restriction of phonon propagation on the lattice thermal conductivity of c-CoSi and c-FeSi, and, as a consequence, on their thermoelectric figure of merit. To reduce the time of theoretical calculations of thermal conductivity for one-dimensional nanostructures compared to two-dimensional ones, the calculation of cobalt and iron monosilicide nanowires was chosen taking into account their directionality in three directions [100], [110] and [111] and then a comparison was made with the data for single crystals with subsequent evaluation of the thermoelectric figure of merit of CoSi and FeSi thin films using the obtained experimental data on the dependence of their power factor on temperature [Fig. 11(c)].

The calculation results in Fig. 12 show that the lattice thermal conductivity of CoSi nanowires depends significantly on the nanowire orientation. Thus, with a diameter of 0.5 nm, the lattice thermal conductivity of the [100] nanowire [Fig. 12(a)] is 25%–33% higher than that of the [111] nanowire [Fig. 11(c)] of the same diameter. However, with an increase in diameter to 26.5 nm, the difference in lattice thermal conductivity reduces to 6%–14%, also decreasing with increasing temperature.

Therefore, when considering nanostructures with significant spatial confinement of phonons, the lattice orientation will not have a significant effect on the lattice thermal conductivity only at characteristic sizes above 26 nm and operating temperatures above 400 K. Calculations show that for nanowires with a diameter of 0.5 nm, the lattice thermal conductivity changes from 2.7% (from 100 K) to 7.6% (up to 400 K) compared to the lattice thermal conductivity of bulk CoSi (Fig. 12). However, with an increase in diameter to 26.5 nm (the maximum in the calculations), the lattice thermal conductivity is already comparable to that of bulk CoSi; from 41% (from 100 K) to 63% (up to 400 K). In the following, when estimating the thermoelectric figure of merit, it is assumed that the lattice thermal conductivity of two-dimensional and thin films is close to that of nanowires, which gives us an upper bound for both CoSi and FeSi films. Such a significant decrease in lattice thermal conductivity is explained by the fact that in bulk CoSi at low temperatures, 90% of the lattice thermal conductivity is provided by phonons with a mean free path greater than 10 nm, and at high temperatures—greater than 3 nm (Fig. 13) and significant scattering of phonons on the surface.

To estimate the contribution of charge carriers to the thermal conductivity ($K_e = \sigma \times L \times T$) in Fig. 12, the Wiedemann–Franz law ($K_e = \sigma \times L \times T$) with the Lorentz

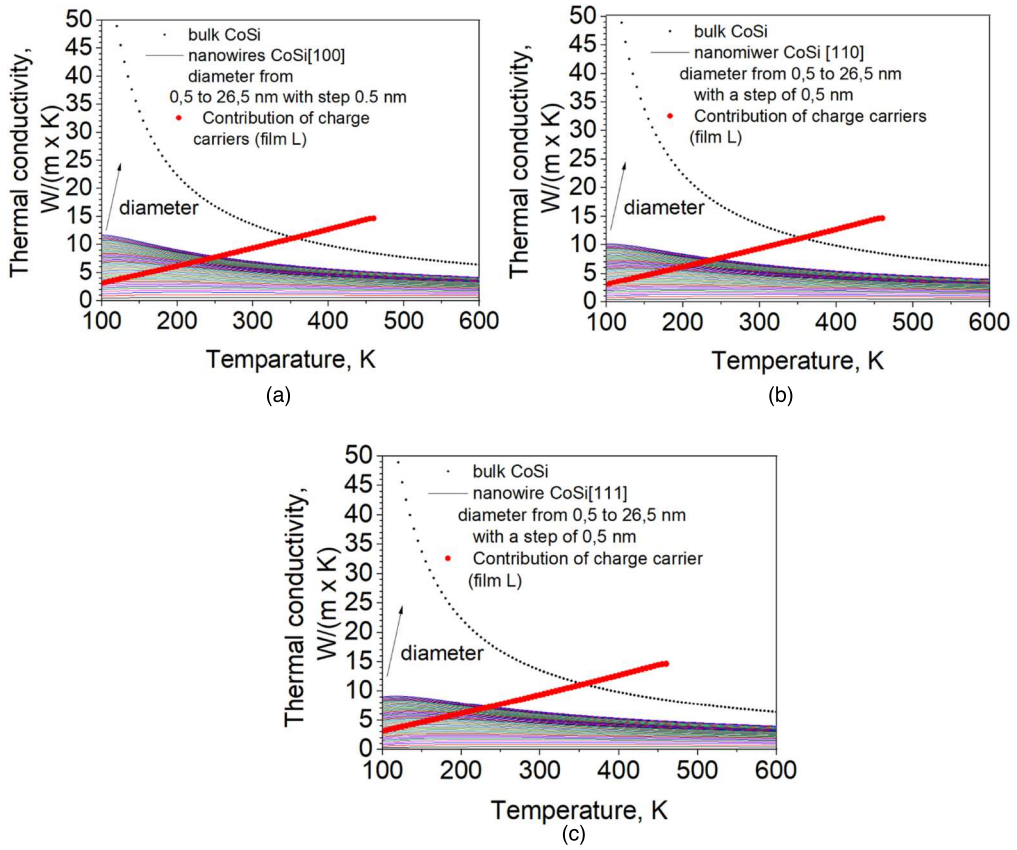

Fig. 12. Calculated lattice thermal conductivity of bulk CoSi along the (100) direction in comparison with nanowires with diameters from 0.5 to 26.5 nm, oriented in the directions: (a) (100) (b) (110) and (c) (111). The contribution of charge carriers to the thermal conductivity is estimated based on the Wiedemann–Franz law and the measured resistivity and calculated power factor [Figs. 11(a), 11(b)].

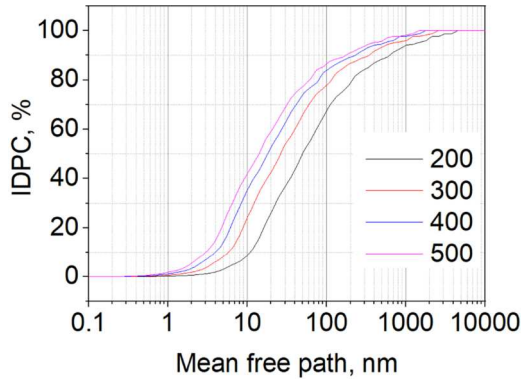

Fig. 13. Integral dependence of the phonon contribution (IDPC) to the lattice thermal conductivity of bulk CoSi on the mean free path at temperatures from 200 to 500 K.

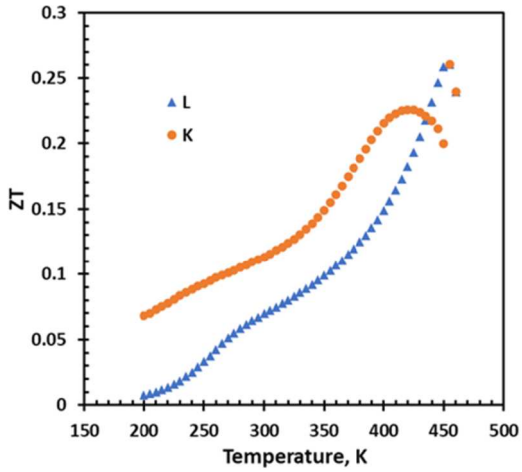

Fig. 14. Temperature dependences of the thermoelectric figure of merit (ZT) of CoSi films in samples K and L.

number value of 2.44×10^{-8} W Ω K^{-2} and the dependence of resistivity on temperature (T) shown in Fig. 11(a) were used for calculation of the electrical conductivity ($\sigma(T)$). It is found (Fig. 12) that for samples L, the contribution of charge carriers to the thermal conductivity becomes comparable to the lattice thermal conductivity at 200 and 300 K, respectively. This indicates that at high temperatures, the main contribution to the thermal conductivity is due to charge carriers, and as a consequence, even a significant further decrease in the lattice thermal conductivity will not provide a noticeable effect.

The obtained values of thermal conductivity from the nanowire diameter (or film thickness) (Fig. 12), electrical conductivity (resistivity [Fig. 11(a)] and the Seebeck coefficient (S) [Fig. 11(b)] were used to estimate the thermoelectric figure of merit ($ZT = (S^2 \times \sigma \times T)/\kappa$). It was found that in the range from 200 to 300 K, the ZT values for both films smoothly increase without reaching saturation (Fig. 14). After 300 K, the ZT value increases sharply and reaches a maximum of 0.225 at 420 K for the c-CoSi film in sample K and then decreases with a further increase in temperature. For the c-CoSi film in sample L, the ZT value increases sharply after 350 K and reaches a maximum of 0.26 at 450 K (Fig. 14). Since the film thicknesses in samples K (13.0 nm (Table I)) and L (14.0 nm [Fig. 1(a)]) are

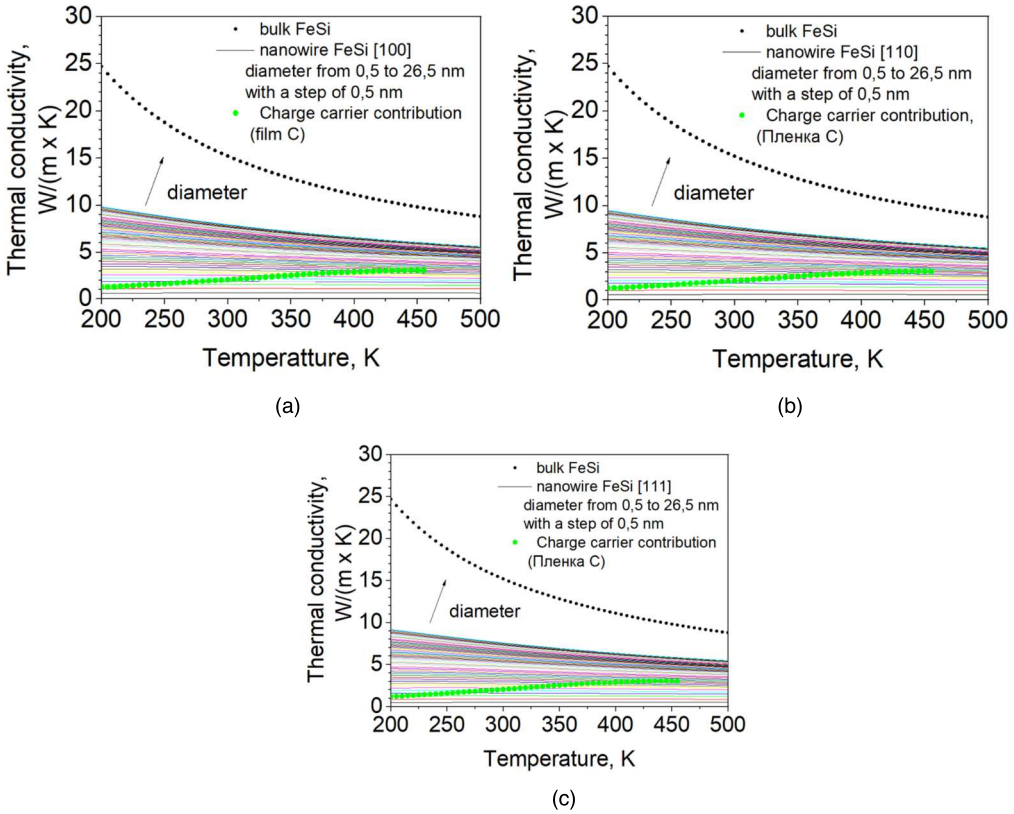

Fig. 15. Calculated lattice thermal conductivity of bulk FeSi along the [100] direction in comparison with nanowires with diameters from 0.5 to 26.5 nm, oriented in the directions: (a) [100], (b) [110] and (c) [111)]. The contribution of charge carriers to the thermal conductivity is estimated based on the Wiedemann–Franz law and the measured resistivity and calculated power factor (Figs. 11(a), 11(b)).

comparable and both films were grown by SPE at 500 °C, a possible reason for the difference in the temperature dependences of the thermoelectric efficiency may be the different orientations of the grains in c-CoSi films on silicon with orientations (111) and (001). Higher roughness for sample *L* (3.0 nm) was found on the Si(111) substrate and lower roughness (1.5 nm) on the substrate with the Si(001) orientation (sample *K*), which is determined by its better crystalline quality (epitaxial) in sample *L*.

The obtained maximum values (0.225 and 0.26) are one and a half to two times higher than the value of $ZT = 0.15$ for bulk undoped CoSi at 450 K.[90] On the other hand, the value of *ZT* obtained in the range from 200 to 350 K significantly exceeds that for the bulk material,[91] which gives grounds to consider CoSi films as a tool that does not require the addition of new types of atoms, which allows expanding the operating range of thermoelectric converters based on bulk CoSi, contributing to an increase in the efficiency of thermoelectric conversion.

To estimate the lattice thermal conductivity of FeSi, ab initio calculations of the phonon structure, group velocity of vibrational modes, phonon scattering velocity, and phonon mean free path were performed for cubic FeSi in both the bulk state (the results obtained are consistent with work[89] and in the form of nanowires in the framework of work.[61] In this work, calculations of the lattice thermal conductivity of cubic FeSi nanowires were performed depending on the orientation of the nanowires and their diameter. The calculation results are shown in Fig. 15 show that the lattice thermal conductivity of cubic FeSi nanowires depends significantly on the orientation in which the nanowire is extended: with a diameter of 0.5 nm, the lattice thermal conductivity of the [100] nanowire is 18%–21% higher than that of the [111] nanowire of the same diameter, but with an increase in diameter to 26.5 nm, the difference in lattice thermal conductivity decreases to 3%–7% (in both cases, the difference decreases with increasing temperature).

By comparing the thermal conductivity of cubic FeSi compared to CoSi it is clear that FeSi shows a weaker dependence of the phonon contribution to the lattice thermal conductivity on the mean free path in FeSi repeats that for CoSi (Fig. 13).

To estimate the thermal conductivity of charge carriers in Fig. 15, the Wiedemann–Franz law with a Lorentz number of 2.44×10^{-8} ($\mathrm{W\,\Omega\,K^{-2}}$) and the temperature dependence of electrical conductivity for c-FeSi films in samples *C* and *D* shown in Fig. 11(a) were also used. The results show that the contribution of charge carriers to the thermal conductivity is comparable with the lattice thermal conductivity at 340 K as in the case of the c-CoSi film [Fig. 11(a)]. Thus, nanostructuring to limit phonon propagation is an effective way to reduce the thermal conductivity of cubic FeSi-based materials.

The estimated *ZT* values for c-FeSi films in a similar way as in the case of c-CoSi films displayed a non-monotonical increase with increasing temperature (Fig. 16) in the range from 200 to 300 K with minimal values for the thinner film (sample *C*, 14.0 nm) as compared to the thicker film (sample *D*, 21.3 nm). With increasing temperature, the *ZT* value for the film in sample *D* reaches saturation at about 280 K, and with a further increase in temperature, a maximum of $ZT = 0.055$ is observed at $T = 430$ K. For the film in sample *C*, in the range 320–380 K a plateau is evident with *ZT* values of ~0.02

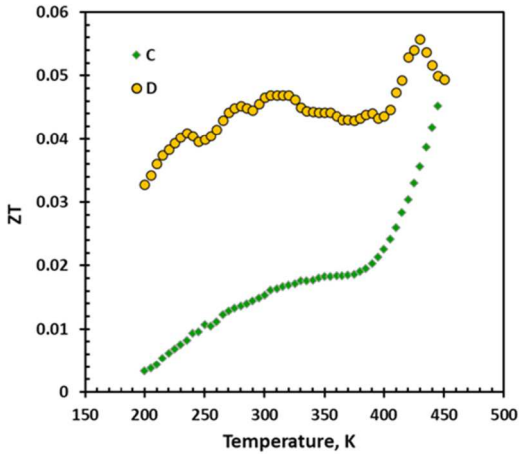

Fig. 16. Temperature dependence of the dimensionless thermoelectric figure of merit (*ZT*) of c-FeSi films in samples *C* and *D*.

followed by a rapid increase of *ZT* to 0.045 at 445 K. The lower values of *ZT* for c-FeSi films compared to c-CoSi films are associated with a significantly lower conductivity of these films even at room temperatures [Fig. 11(a)] at close values of the Seebeck coefficient [Fig. 11(b)]. Since the films were grown by MBE at the same temperature (350 °C) on a substrate with the same orientation (Si(111)), but have different thicknesses, and the crystalline quality is better in the film in sample *D*.[12] That is, in a thicker c-FeSi film of better crystalline quality, the Seebeck coefficient is larger in amplitude and depends only slightly on the thickness. The obtained maximum values of the thermoelectric figure of merit (Fig. 16) in the temperature range of 250–300 K are approximately four times larger than the values obtained for the bulk material in indicating that c-FeSi epitaxial films look more promising as a basis for low-temperature thermoelectric converters than cubic FeSi bulk.[89]

4. Conclusions

(1) UT (3–4 nm) and thin (13–66 nm) FeSi, CrSi and CoSi films were grown on Si(111) and Si(100) substrates by solid-phase and MBE methods under ultrahigh vacuum conditions at 350 and 450 °C–500 °C. For the first time, a monoclinic phase was detected for UT m-FeSi and m-CrSi films, which transforms into a cubic phase with increasing film thickness. In CoSi films, regardless of the thickness, only a cubic phase is formed, which is confirmed by HRTEM data.

(2) Temperature measurements of the conductivity of UT films of m-FeSi, m-CrSi and c-CoSi were carried out. The temperature range of 2–30 K was determined for them, where there is no shunting by the silicon substrate. It was found that the UT films have two-dimensional conductivity, which was confirmed by agreement with the model of a two-dimensional electron gas in a non-activated quasi-metallic medium with the effects of electron–electron interaction and disorder. A higher layer conductivity of cubic phases of iron and chromium monosilicides was established compared to monoclinic phases in UT m-FeSi and m-CrSi films.

(3) Low-temperature magnetoresistance measurements for UT m-FeSi, m-CrSi and c-CoSi films and its thin films in magnetic fields from 0.25 to 8.0 T revealed two effects. At temperatures below 30 K for UT m-FeSi and c-CoSi films, regions of negative MR, positive MR and their crossovers are observed at different magnetic fields, which is associated with the excitation of weak localization and antilocalization processes. Weak localization and antilocalization effects are also retained in thin c-FeSi films with the appearance of a linear NMR from the magnetic field at $T = 30$ K. For the UT m-CrSi film at $T = 2$ K, a linear dependence of MR_{xx} on the magnetic field is observed, which corresponds to the implementation of the Abrikosov model of quantum magnetoresistance in low magnetic fields.

(4) In thin c-CoSi films, an increase in electron–electron interactions was observed at temperatures from 2 to 30 K, which may be due to surface-dominated transport caused by topological phenomena. In ultra-high-temperature m-FeSi and m-CrSi films, no topological effects were observed.

(5) Based on the slope of the field dependences of the Hall resistance of the UT m-CrSi and c-CoSi films in the temperature range of 2–30 K, it was determined that the main carriers in its are: holes for m-CrSi and electrons for c-CoSi. It was established that in the temperature range of 2–30 K for these films, the normal Hall effect was confirmed, the range of changes in the concentration of holes in m-CrSi and m-FeSi (7×10^{19}–6×10^{22} cm^{-3})) and electrons in c-CoSi ($(2–7) \times 10^{21}$ cm^{-3}) and their dependence on temperature and magnetic field were determined.

(6) Magnetic properties of UT (m-FeSi and m-CrSi) and thin c-FeSi and (m-CrSi + c-CrSi) films of and the first studied UT and thin c-CoSi films were compared and it was found that they exhibit weak ferromagnetic or antiferromagnetic properties (UT m-CrSi films), which are not inherent in bulk monosilicides. For m-FeSi and c-CoSi films, there are two experimental facts: (1) observation of ferromagnetic loops from ultralow temperature (3–4 K) to room temperature (300 K) with a coercive force close to zero, which is typical for superparamagnets and (2) the appearance of a blocking temperature with a broadened shape on the FC curves associated with the size distribution of magnetic nanoparticles. At a temperature of 4 K, a noticeable coercive force and a residual magnetic moment characteristic of magnetic domains appear for m-FeSi and c-CoSi films, which does not allow us to classify the films under consideration as classical superparamagnets and requires additional studies.

(7) Thermoelectric properties were studied only for thin FeSi, CrSi and CoSi films, which have noticeable conductivity and different conductivity dependences on temperature from silicon, which allowed us to use a two-layer thermoelectric power model for calculations. Thin films of c-CrSi (20–80 nm) have metallic conductivity and a positive Seebeck coefficient and a power factor from 0.7 to 1.0 mW m^{-1} K^{-2}). Thin films of c-FeSi and c-CoSi have semi-metallic conductivity with moderate conductivity and demonstrate a maximum power factor: (2.5–2.8) mW m^{-1} K^{-2} in the temperature range from 200 to 400 K and require additional research.

(8) For bulk samples and FeSi and CoSi nanowires, ab initio calculations of lattice thermal conductivity were performed in comparison with its value in single crystals, the influence of the FeSi and CoSi nanowire direction on the lattice thermal conductivity was established, and the range of nanowire diameters (0.5–10 nm) was determined, when it decreases by at least 8 times. Using the lattice thermal conductivity calculation data and experimental data on the power factor, it was possible to calculate the thermoelectric figure of merit (ZT) from temperature for thin FeSi and CoSi films. Estimates of the maximum achievable ZT value showed the following values in the temperature range of 340–450 K: 0.26 for CoSi thin films without additional doping and 0.05–0.055 for FeSi thin films.

(9) It is shown that in the temperature range of 200–400 K, thin CoSi films without additional doping with $ZT = 0.10$–0.26 and thin FeSi films with $ZT = 0.05$–0.055 on single-crystal silicon can be promising for creating, respectively, electron and hole branches in a thermoelectric converter for the Internet of Things (IoT).

(10) Potential applications in spintronics have been proposed for UT and thin films of FeSi, CrSi and CoSi.

Acknowledgments

All researches were carried out within the state assignment of IACP FEB RAS (Theme FWFW-2021–0002). Calculations of phonon band structures and thermal conductivity were performed using the equipment of the Far Eastern Computing Resource Center at the Institute of Automation and Control Processes, Far Eastern Branch of the Russian Academy of Sciences (https://cc.dvo.ru) and the Academician V.M. Matrosov computing cluster (https://hpc.icc.ru). High-resolution transmission electron microscopy studies were carried out using the equipment at the Institute of Nanotechnology of Microelectronics of the Russian Academy of Sciences. X-ray and magnetic measurements were performed using the equipment at the Institute of Chemistry, Far Eastern Branch of the Russian Academy of Sciences.

Appendix

We insert three Appendixes, which are labeled as appendix A (XRD data for thin CoSi film grown on single-crystal silicon by SPE and MBE methods at $T = 350$ °C) and appendix B (dependences of electron concentration versus temperature (3–300 K) and magnetic induction (0.25–7.5 T) in the UT CrSi film).

ORCID iDs

Nikolay G. Galkin https://orcid.org/0000-0003-4127-2988
Oleg V. Kropachev https://orcid.org/0000-0003-4300-0070
Aleksandr A. Dudin https://orcid.org/0000-0001-7617-8815

1) Z. Schlesinger, Z. Fisk, H.-T. Zhang, M. B. Maple, J. F. DiTusa, and G. Aeppli, Phys. Rev. Lett. **71**, 1748 (1993).
2) L. Degiorgi, M. B. Hunt, H. R. Ott, M. Dressel, B. J. Feenstra, G. Gruner, Z. Fisk, and P. Canfield, Europhys. Lett. **28**, 341 (1994).
3) A. Damascelli, K. Schulte, D. Van der Marel, and A. A. Menovsky, Phys. Rev. B **55**, R4863 (1997).
4) M. Fäth, J. Aarts, A. A. Menovsky, G. J. Nieuwenhuys, and J. A. Mydosh, Phys. Rev. B **58**, 15483 (1998).
5) P. Samuely, P. Szabó, M. Mihalik, N. Hudáková, and A. A. Menovsky, Physica B **218**, 185 (1996).
6) V. Jaccarino, G. K. Wertheim, J. H. Wernick, L. R. Walker, and S. Arajs, Phys. Rev. **160**, 476 (1967).
7) G. Aeppli et al., Comments Condens. Matter Phys. **16**, 155 (1992).
8) A. Lacerda, H. Zhang, P. C. Canfield, M. F. Hundley, Z. Fisk, J. D. Thompson, C. L. Seaman, M. B. Maple, and G. Aeppli, Physica B **186–188**, 1043 (1993).
9) K. Breuer, S. Messerli, D. Purdie, M. Garnier, M. Hengsberger, Y. Baer, and M. Mihalik, Phys. Rev. B **56**, R7061 (1997).
10) K. Tajima, Y. Endoh, J. E. Fischer, and G. Shirane, Phys. Rev. B **38**, 6954 (1988).
11) J. Beille, J. Voiron, and M. Roth, Solid State Commun. **47**, 399 (1983).
12) N. G. Galkin et al., J. Surf. Investig.: X-ray, Synchr. Neutron Tech. **18**, 372 (2024).
13) R. A. Smith, *Semiconductors* (Cambridge University Press, Cambridge, 1978) 2nd ed.436.
14) E. Bauer, S. Bocelli, R. Hauser, F. Marabelli, and R. Spolenak, Physica B **230-232**, 794 (1997).
15) Y. Takahashi, M. Tano, and T. Moriya, J. Magn. Magn. Mater. **31**, 329 (1983).
16) S. N. Evangelou and D. M. Edwards, J. Phys. C **16**, 2121 (1983).
17) Z. Fisk et al., Physica B **206–207**, 798 (1995).
18) C. M. Varma, Phys. Rev. B **50**, 9952 (1994).
19) C. Fu and S. Doniach, Phys. Rev. B **51**, 17439 (1995).
20) V. I. Anisimov, S. Y. Ezhov, I. S. Elfimov, I. V. Solovyev, and T. M. Rice, Phys. Rev. Lett. **76**, 1735 (1996).
21) T. Jarlborg, Phys. Rev. Lett. **77**, 3693 (1996).
22) S. Zeng, J. Tian, X. Han, Y. Meng, M. Zhu, and H. Zhang, J. Nucl. Mater. **558**, 153310 (2022).
23) F. Wu, A. W. McLaurin, K. E. Henson, D. G. Managhan, and S. L. Thomasson, Thin Solid Films **332**, 418 (1998).
24) P. Wetzel, C. Pirri, J. C. Peruchetti, D. Bolmont, and G. Gewinner, Solid State Commun. **65**, 1217 (1988).
25) L. F. Bates and A. Baqi, Proc. Phys. Soc. **48**, 781 (1936).
26) E. W. Collings, F. T. Hedgcock, and A. Siddiqi, Phil. Mag. **6**, 155 (1961).
27) S. Banik, M. K. Chattopadhyay, S. Tripathi, R. Rawat, and S. N. Jha, Sci. Rep. **10**, 12030 (2020).
28) I. E. Dzyaloshinskii, J. Phys. Chem. Solids **4**, 241 (1958).
29) T. Moriya, Phys. Rev. **120**, 91 (1960).
30) N. G. Galkin, D. L. Goroshko, A. V. Konchenko, V. A. Ivanov, E. S. Zakharova, and S. T. Krivoshchapov, Surf. Rev. Lett. **7**, 257 (2000).
31) N. G. Galkin, D. L. Goroshko, A. V. Konchenko, V. A. Ivanov, and A. S. Gouralnik, Surf. Rev. Lett. **6**, 7 (1999).
32) N. G. Galkin, A. V. Konchenko, D. L. Goroshko, A. M. Maslov, S. V. Vavanova, and S. I. Kosikov, Appl. Surf. Sci. **166**, 113 (2000).
33) N. G. Galkin, D. L. Goroshko, S. T. Krivoshchapov, and E. S. Zakharova, Appl. Surf. Sci. **175-176**, 230 (2001).
34) V. A. Gasparov, V. A. Grazhulis, V. V. Bondarev, T. M. Bychkova, V. G. Lifshits, N. G. Galkin, and N. I. Plusnin, Surf. Sci. **292**, 298 (1993).
35) Y. Imai, M. Mukaida, K. Kobayashi, and T. Tsunoda, Intermetallics **9**, 261 (2001).
36) D. A. Pshenay-Severin and A. T. Burkov, Materials **12**, 2710 (2019).
37) P. Dutta and S. K. Pandey, Comput. Condens. Matter **16**, e0035 (2018).
38) P. Tang, Q. Zhou, and S. C. Zhang, Phys. Rev. Lett. **119**, 206402 (2017).
39) D. A. Pshenay-Severin, Y. V. Ivanov, A. A. Burkov, and A. T. Burkov, J. Phys. Condens. Matter **30**, 135501 (2018).
40) D. Takane et al., Phys. Rev. Lett. **122**, 076402 (2019).
41) G. Chang, S. Y. Xu, B. J. Wieder, D. S. S. S. M. Huang, I. Belopolski, T. R. Chang, S. Zhang, A. Bansil, H. Lin, and M. Z. Hasan, Phys. Rev. Lett. **119**, 206401 (2017).
42) Z. Rao et al., Nature **567**, 496 (2019).
43) D. S. Sanchez et al., Nature **567**, 500 (2019).
44) J. S. Tsay, C. S. Yang, Y. Liou, and Y. D. Yao, J. Appl. Phys. **85**, 4967 (1999).
45) K. Adachi, K. Ito, L. Zhang, and M. Yamaguchi, Marer. Sci. Forum **426-432**, 3445 (2003).
46) V. S. Kuznetsovaa, S. V. Novikova, C. K. Nichenametlab, J. Calvob, and M. Wagner-Reetzb, Semiconductors **53**, 775 (2019).
47) C. K. Nichenametla et al., Allg. Chem. **646**, 1231 (2020).
48) A. Molinari et al., ACS Appl. Electron. Mater. **5**, 2624 (2023).
49) Z. Li, Y. Yuan, R. Hübner, L. Rebohle, Y. Zhou, M. Helm, K. Nielsch, S. Prucnal, and S. Zhou, ACS Appl. Mater. Interfaces **15**, 30517 (2023).
50) M. T. Normuradov, I. R. Bekpulatov, G. T. Imanova, and B. D. Igamov, Adv. Phys. Res. **4**, 142 (2022).
51) L. Rocchino, A. Molinari, I. Kladaric, F. Balduini, H. Schmid, M. Sousa, J. Bruley, H. Bui, B. Gotsmann, and C. B. Zota, Sci. Rep. **14**, 20608 (2024).

52) Z. Pan, L. Zhang, and J. Wu, J. Appl. Phys. **101**, 033715 (2007).
53) A. Sakai, F. Ishii, Y. Onose, Y. Tomioka, S. Yotsuhashi, H. Adachi, N. Nagaosa, and Y. Tokura, J. Phys. Soc. Jpn. **76**, 093601 (2007).
54) T. Ou-Yang, Y. Zhuang, B. Ramachandran, W. Chen, G. Shu, C. Hu, F. Chou, and Y. Kuo, J. Alloys Compd. **702**, 92 (2017).
55) D. A. Pshenay-Severin, Y. V. Ivanov, A. T. Burkov, S. V. Novikov, V. K. Zaitsev, and H. Reith, J. Electron. Mater. **47**, 3277 (2018).
56) A. T. Burkov, S. V. Novikov, V. K. Zaitsev, and H. Reith, Semiconductors **51**, 689 (2017).
57) N. G. Galkin et al., Comput. Mater. Sci. **233**, 112762 (2024).
58) N. G. Galkin, K. N. Galkin, O. V. Kropachev, S. A. Dotsenko, D. L. Goroshko, D. B. Migas, A. B. Filonov, N. V. Skorodumova, A. V. Gerasimenko, and A. K. Gutakovskii, J. Mater. Chem. C **13**, 2987 (2025).
59) N. G. Galkin, E. Y. Subbotin, K. N. Galkin, D. L. Goroshko, O. A. Goroshko, D. B. Migas, A. B. Filonov, I. A. Tkachenko, and A. Y. Samardak, J. Mater. Chem. C **13**, 2875 (2025).
60) K. N. Galkin, I. M. Chernev, E. Y. Subbotin, A. M. Maslov, O. V. Kropachev, D. L. Goroshko, S. A. Balagan, E. V. Argunov, A. K. Gutakovsky, and N. G. Galkin, St. Petersburg State Polyt. Univ. J.: Phys. Math. **16**, 84 (2023).
61) S. A. Balagan and N. G. Galkin, St. Petersburg Polyt. Univ. J.: Phys. Math. **17**, 111 (2024).
62) D. L. Goroshko, K. N. Galkin, I. M. Chernev, A. M. Maslov, O. V. Kropachev, E. Yu. Subbotin, O. A. Goroshko, and N. G. Galkin, St. Petersburg Polyt. Univ. J.: Phys. Math. **17**, 25 (2024).
63) D. L. Goroshko et al., IEEE Xplore **287**, 10755921 (2024).
64) CrystalMaker Software http://crystalmaker.com/.
65) https://gatan.com/products/tem-analysis/gatan-microscopy-suite-software.
66) J. H. Bahk, T. Favaloro, and A. Shakouri, Ann. Rev. Heat Trans. **16**, 30 (2013).
67) M. Liehr, M. Renier, R. A. Wachnik, J. Werner, S. G. Scilla, and P. S. Ho, J. Vac. Sci. Technol. A **5**, 2131 (1987).
68) G. Kresse and J. Furthmüller, Comput. Mater. Sci. **6**, 15 (1996).
69) B. Boren, Mineralogi och Geologi A **11**, 2 (1933).
70) A. Togo and I. Tanaka, Scr. Mater. **108**, 1 (2015).
71) W. Li, J. Carrete, N. A. Katcho, and N. Mingo, Comp. Phys. Commun. **185**, 1747 (2014).
72) T. Ando, A. B. Fowler, and F. Stern, Rev. Mod. Phys. **54**, 527 (1982).
73) N. E. Hussey, K. Takenaka, and H. Takagi, Phil. Mag. **84**, 2847 (2004).
74) B. L. Altshuler, A. G. Aronov, and P. A. Lee, Phys. Rev. Lett. **44**, 1288 (1980).
75) H. Fukuyama, J. Phys. Soc. Jpn. **50**, 3407 (1981).
76) P. F. Maldague, Phys. Rev. B **3**, 1719 (1981).
77) J. L. Olsen, *Electron Transport in Metals* (Interscience, New York, 1962).
78) A. A. Abrikosov, Europhys. Lett. **49**, 789 (2000).
79) F. Y. Yang et al., Science **284**, 1335 (1999).
80) J. Hu and T. F. Rosenbaum, Nat. Mater. **7**, 697 (2008).
81) P. J. Newton, R. Mansell, S. N. Holmes, M. Myronov, and C. H. W. Barnes, Appl. Phys. Lett. **110**, 062101 (2017).
82) G. C. Papaefthymiou, Nano Today **4**, 438 (2009).
83) J. A. Mydosh, Rep. Prog. Phys. **78**, 052501 (2015).
84) E. Sonder and D. K. Stevens, Phys. Rev. **110**, 1027 (1958).
85) Y. Kousaka, Y. Takahashi, N. Ikeda, H. Matsui, J.-I. Kishine, Y. Togawa, M. Miyagawa, S. Nishihara, K. Inoue, and J. Akimitsu, JPS Conf. Proc. **3**, 014037 (2014).
86) K. P. Misra et al., Nanoscale Adv. **6**, 3838 (2024).
87) S. Mandal, K. S. R. Menon, S. K. Mahatha, and S. Banerjee, Appl. Phys. Lett. **99**, 232507 (2011).
88) K. Yosida, Phys. Rev. **106**, 893 (1957).
89) R. Stern, T. Wang, J. Carrete, N. Mingo, and G. K. H. Madsen, Phys. Rev. B **97**, 195201 (2018).
90) M. Ioannou, E. Symeou, J. Giapintzakis, and T. Kyratsi, J. Electron. Mater. **43**, 3824 (2014).
91) T. Y. Ou-Yang, G. J. Shu, and H. R. Fuh, Europhys. Lett. **120**, 17002 (2017).